J. Fluid Mech. (2020), *vol.* 893, A21. © The Author(s), 2020.
Published by Cambridge University Press
doi:10.1017/jfm.2020.246

Surface wave effects on energy transfer in overlying turbulent flow

Li-Hao Wang[1], Wu-Yang Zhang[1], Xuanting Hao[2], Wei-Xi Huang[1,†], Lian Shen[2], Chun-Xiao Xu[1] and Zhaoshun Zhang[1]

[1]Applied Mechanics Laboratory, Department of Engineering Mechanics, Tsinghua University, Beijing 100084, China

[2]Department of Mechanical Engineering and Saint Anthony Falls Laboratory, University of Minnesota, Minneapolis, MN 55455, USA

(Received 7 July 2019; revised 29 December 2019; accepted 23 March 2020)

Phase-resolved wave simulation and direct numerical simulation of turbulence are performed to investigate the surface wave effects on the energy transfer in overlying turbulent flow. The JONSWAP spectrum is used to initialize a broadband wave field. The nonlinear wave field is simulated using a high-order spectral method, and the resultant wave surface provides the bottom boundary conditions for direct numerical simulation of the overlying turbulent flow. Two wave ages of $c_p/u_* = 2$ and 25 are considered, corresponding to slow and fast wave fields, respectively, where c_p denotes the celerity of the peak wave and u_* denotes the friction velocity. The energy transfer of turbulent motions in the presence of surface waves is investigated through the spectral analysis of the two-point correlation transport equation. It is found that the production term has an extra peak at the dominant wavelength scale in the vicinity of the surface, and the energy transported to the surface via viscous and spatial turbulent transport is enhanced in the region of $y^+ < 10$. The presence of surface waves results in an inverse turbulent energy cascade in the near-surface region, where small-scale wave-related motions transfer energy back to the dominant wavelength scale. Pressure-related terms reflecting the spatial and inter-component energy transfer are strongly dependent on the wave age. Furthermore, triadic interaction analysis reveals that the energy influx at the dominant wavelength scale is due to the contribution of the neighbouring streamwise turbulent motions, and those at the harmonic wavelength scales contribute the most.

Key words: turbulence simulation, turbulent boundary layers, wind–wave interactions

1. Introduction

Energy transfer is a fundamental process in turbulence. It is closely related to the multi-scale feature and spatial inhomogeneity of turbulent flows. In the description of the energy cascade process (Richardson 1922), the successive energy transfer

† Email address for correspondence: hwx@tsinghua.edu.cn

https://doi.org/10.1017/jfm.2020.246 Published online by Cambridge University Press

from large to small scales was exhibited. Under the assumption of homogeneity and isotropy, the asymptotic statistics of small-scale motions at very high Reynolds numbers were obtained by Kolmogorov (1941*a*), e.g. the scaling of the moments of velocity increments. In addition, the energy cascade among different length scales is described by the Kolmogorov equation (Kolmogorov 1941*b*), where the unidirectional energy flux from large to small scales is related to the averaged dissipation rate. After Kolmogorov's pioneering work, many efforts have been devoted to the study of the multi-scale behaviour of turbulent flows (e.g. Kraichnan 1971; Meneveau & Katz 2000; Vassilicos 2015; Dubrulle 2019).

Compared with homogeneous turbulence, the energy transfer process becomes more complex in wall-bounded turbulent flows due to spatial inhomogeneity. Starting from the two-point correlation transport equation, Lumley (1964) analysed the spectral energy budget in wall-bounded turbulence and deduced that inverse energy transfer occurs due to the energy and pressure fluxes in the wall-normal direction. In the past few decades, direct numerical simulation (DNS) has provided evidence for the existence of the inverse energy cascade. Domaradzki *et al.* (1994) observed inverse energy transfer and showed the scale locality of the energy cascade in low-Reynolds-number wall-bounded turbulent flows. Using DNS data up to $Re_\tau = 5200$, where Re_τ is the friction Reynolds number based on the friction velocity and channel half-width, Lee & Moser (2015) performed a spectral analysis of the terms in the transport equation of the two-point velocity correlation and also observed inverse energy transfer. Cho, Hwang & Choi (2018) visualized the triadic interactions involved in the turbulent energy transport in a turbulent channel flow of $Re_\tau = 1700$ to illustrate the existence of energy transfer from small- to large-scale motions, but the classical energy cascade was found still to be the dominant transfer mechanism. Recently, Mizuno (2016) revealed the scale dependence of spatial turbulent kinetic energy transport in a channel flow up to $Re_\tau = 1000$. The downward energy flux at large scales was found to be responsible for the Reynolds number dependence of turbulence intensity. Later, Lee & Moser (2019) observed the same phenomenon from their $Re_\tau = 5200$ DNS dataset, and further studied the interaction between the near-wall dynamics and the outer-layer turbulence dominated by very-large-scale motions. In the above studies, the inter-scale energy transfer in the wall-parallel directions and the spatial energy transport in the wall-normal direction were the main concern, and the wall-normal scales were not considered.

While in the studies mentioned above spectral analyses were applied to the homogeneous wall-parallel plane to extract the scale dependence of energy transfer, the statistics in physical space may provide further insight. Hill (2002) derived the balance equation for the second-order structure function in anisotropic turbulence to establish the relation between the second- and third-order moments, which can be physically interpreted as the scale energy and the scale-energy flux, respectively. Using the generalized Kolmogorov equation, Marati, Casciola & Piva (2004) evaluated the scale-by-scale balance in different regions of a channel flow. Along this line, Cimarelli, De Angelis & Casciola (2013) observed an ascending spiral-like energy transfer path in the combined space of wall-parallel scales and wall-normal distance. They found that the inverse energy cascade plays a key role in the formation of the very long streaks of velocity fluctuations. Later, the generalized Kolmogorov equation was further studied by Cimarelli *et al.* (2016) in the reduced space of wall-normal and spanwise scales and wall-normal distance.

While considerable progress has been made in understanding the energy transfer in canonical wall-bounded turbulent flows as reviewed above, there has been much

https://doi.org/10.1017/jfm.2020.246 Published online by Cambridge University Press

less work on the energy transfer process in wall-bounded turbulence with a travelling wavy boundary, for instance, in the framework of wind–wave interaction (Sullivan & McWilliams 2010). Surface waves carry a new energy source and multi-scale waving motions, which may significantly affect the energy transfer process in the overlying turbulent flow. In the early years, several theoretical models, e.g. the resonance mechanism (Phillips 1957) and the critical layer theory (Miles 1957), were proposed to explain the wind–wave generation process and to predict the wave growth rate. Later, Belcher & Hunt (1993) and Cohen & Belcher (1999) performed analyses of the non-separated sheltering phenomenon of slow- and fast-moving waves, respectively, based on the rapid distortion theory, to explain the momentum transfer between airflow and surface waves. In recent years, laboratory measurements and field observations have provided valuable flow-field data, which yield important insights into the physical process of wind–wave interaction. For example, using laboratory measurements, Buckley & Veron (2016, 2019) obtained the instantaneous and phase-averaged velocity fields of the airflow above surface waves for different wind–wave conditions. Meanwhile, field observations in open sea provide data of the flow field at the air–sea interface over a wide range of scales. In Black *et al.* (2007), air–sea exchange measurements were conducted to improve the parameterization of weather forecast models, such as hurricane intensity. In Hristov, Miller & Friehe (2003) and Grare, Lenain & Melville (2013), evidences of the Miles critical layer theory were obtained from field observations.

With the rapid increase in computing power and advances in algorithm development, numerical simulation has become a useful tool for studying wind–wave interactions. Based on the DNS data of turbulent airflows over idealized water waves, the waves were found to have significant influence on the mean flow, vertical momentum transfer, form drag, coherent structures, scalar transport and very-large-scale motions in the air (Sullivan, McWilliams & Moeng 2000; Kihara *et al.* 2007; Yang & Shen 2009; Druzhinin, Troitskaya & Zilitinkevich 2012; Yang & Shen 2017; Zhang, Huang & Xu 2019), and the effects depend on the water wave properties, including the wave steepness, wave age, wave nonlinearity and wind-induced surface drift (e.g. Yang & Shen 2010). In addition to the monochromatic travelling wave as an idealized case, the broadband wave field containing multi-scale wave motions is a more realistic representation of the sea condition. However, there are fewer studies of the interaction between broadband waves and wind turbulence due to the additional complexity associated with an irregular wave system over a wide range of scales. Liu *et al.* (2010) adopted the high-order spectral (HOS) method (Dommermuth & Yue 1987) for simulating the dynamic evolution of broadband nonlinear waves under wind forcing and quantified the wave growth rate for different wave components. They found that the wave growth rate can be approximated by the corresponding monochromatic components for long waves, while stochastic modelling is called for in the case of short waves. Sullivan, McWilliams & Patton (2014) performed large-eddy simulation of wind turbulence over a broadband spectrum of moving waves, and observed that the wind profile deviates from the Monin–Obukhov similarity theory under non-equilibrium wind–wave conditions. Very recently, Hao & Shen (2019) studied wind turbulence over broadband waves with a focus on the long-term evolution of the nonlinear wave field. As an application, Yang, Meneveau & Shen (2014) investigated an offshore wind farm under different wind–sea conditions, and observed that the fully developed wind–sea condition induces less resistance to the wind as compared with the fetch-limited wind–sea condition, and has more wind energy available to harvest.

https://doi.org/10.1017/jfm.2020.246 Published online by Cambridge University Press

The aim of the present work is to investigate the turbulent energy transfer process under the impact of broadband waves. Because the surface waves can affect the turbulent coherent structures and momentum transfer, the scale and spatial characteristics of the energy transfer process may differ appreciably from those in canonical wall-bounded turbulent flows. For this purpose, the HOS method is adopted to capture the nonlinear multi-scale water wave motions. The HOS method has been validated extensively in previous studies (Dommermuth & Yue 1987; Tanaka 2001; Xiao *et al.* 2013). The overlying three-dimensional, instantaneous airflow data are obtained using DNS, which is coupled to the wave simulation through the air–sea boundary conditions following Yang & Shen (2010, 2011). From the DNS data, unique features of the airflow over both slow and fast wave fields are identified from the instantaneous turbulent flow field and the turbulence statistics, such as the turbulent energy spectrum. Furthermore, spectral analysis of the two-point correlation transport equation in curvilinear coordinates is performed to reveal the energy transfer process in the flow over broadband waves. Here, the focus of study is on the surface wave effects on the energy transfer process among different length scales in spectral space and different vertical locations in physical space, which is important for improving the parameterization of surface wave effects on marine atmospheric surface layers (Black *et al.* 2007; Edson *et al.* 2007; Chen *et al.* 2013; Breivik *et al.* 2015). The rest of this paper is organized as follows. The problem formulation and numerical method are briefly introduced in § 2. The instantaneous flow field, energy spectrum and detailed analyses of the energy transfer process are presented in § 3. Finally, conclusions are drawn in § 4.

2. Problem formulation and numerical method

The problem under consideration is a fully developed three-dimensional turbulent flow over water waves. As shown in figure 1, the fluid motion is defined in the Cartesian coordinates (x_1, x_2, x_3), or equivalently (x, y, z), where x, y and z denote the streamwise, vertical and spanwise directions, respectively. The water wave motions are assumed to be irrotational with periodic boundary conditions. The initial wave field is prescribed based on a broadband wave spectrum. At the peak (denoted by subscript 'p') wavenumber (k_p) of the wave spectrum, the corresponding wave parameters depicted in figure 1 are the wavelength (λ_p) and the phase speed (c_p).

2.1. *Governing equations*

The governing equations for the turbulent flow are the dimensionless incompressible Navier–Stokes equations and the continuity equation:

$$\frac{\partial \boldsymbol{u}}{\partial t} + \boldsymbol{u}\cdot\nabla\boldsymbol{u} = -\nabla p + \frac{1}{Re}\nabla^2\boldsymbol{u}, \tag{2.1}$$

$$\nabla\cdot\boldsymbol{u} = 0, \tag{2.2}$$

where $\boldsymbol{u} = (u_1, u_2, u_3)$ or equivalently (u, v, w) denotes the flow velocity vector, p is the dynamic pressure normalized by ρU_m^2 and $Re = U_m\delta/\nu$ is the bulk Reynolds number, with U_m being the bulk velocity, ν the kinematic viscosity and δ the channel half-width.

The DNS of the turbulent flow is carried out using the pseudo-spectral method based on a boundary-fitted mesh (Ge, Xu & Cui 2010; Zhang *et al.* 2019). For this purpose, with a strategy similar to that applied in previous studies (Choi, Moin & Kim

https://doi.org/10.1017/jfm.2020.246 Published online by Cambridge University Press

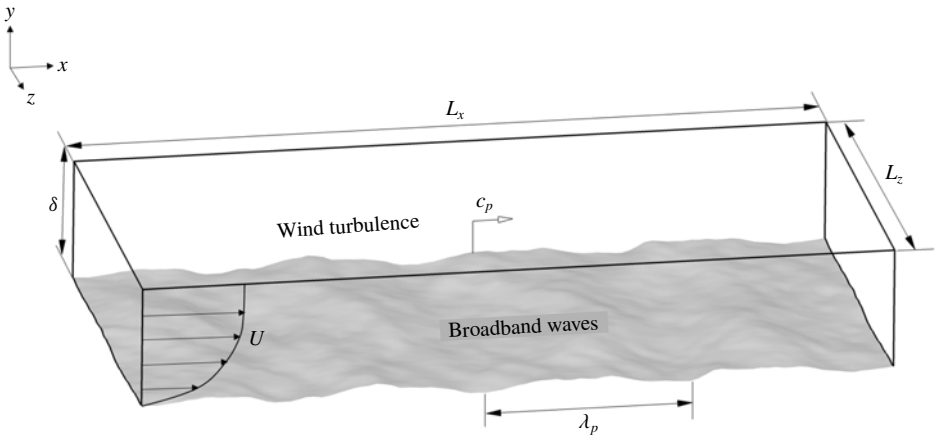


FIGURE 1. Sketch of a three-dimensional turbulent flow over water waves.

1993; Sullivan *et al.* 2000; Hara & Sullivan 2015; Husain *et al.* 2019), the governing (2.1) and (2.2) are transformed into the computational domain by introducing an algebraic mapping:

$$t = \tau, \quad x_1 = \xi_1, \quad x_2 = \xi_2(1 - \eta/\delta) + \eta, \quad x_3 = \xi_3, \tag{2.3a–d}$$

where ξ_1, ξ_2, ξ_3 and τ are the space and time coordinates in the computational domain and η is the wave surface elevation. Then the governing equations (2.1) and (2.2) are rewritten as follows (Kang & Choi 2000):

$$\frac{\partial u_i}{\partial \tau} = -\frac{\partial u_i u_j}{\partial \xi_j} - \phi_j \frac{\partial u_i u_j}{\partial \xi_2} - \frac{\partial p}{\partial \xi_i} + \frac{1}{Re}\frac{\partial^2 u_i}{\partial \xi_j \partial \xi_j} - \phi_t \frac{\partial u_i}{\partial \xi_2} - \phi_i \frac{\partial p}{\partial \xi_2} + \frac{1}{Re} S(u_i), \tag{2.4}$$

$$\frac{\partial u_i}{\partial \xi_i} = -\phi_j \frac{\partial u_j}{\partial \xi_2}, \tag{2.5}$$

where

$$S(u_i) = 2\phi_j \frac{\partial^2 u_i}{\partial \xi_j \partial \xi_2} + \frac{\partial u_i}{\partial \xi_2}\frac{\partial \phi_j}{\partial \xi_j} + \phi_j \frac{\partial \phi_j}{\partial \xi_2}\frac{\partial u_i}{\partial \xi_2} + \phi_j \phi_j \frac{\partial^2 u_i}{\partial \xi_2 \partial \xi_2}, \tag{2.6}$$

$$\left.\begin{aligned} \phi_t &= \frac{\partial \xi_2}{\partial t} = \frac{1}{\delta - \eta}\left(\xi_2 \frac{\partial \eta}{\partial \tau} - \delta \frac{\partial \eta}{\partial \tau}\right), \\ \phi_1 &= \frac{\partial \xi_2}{\partial x_1} = \frac{1}{\delta - \eta}\left(\xi_2 \frac{\partial \eta}{\partial \xi_1} - \delta \frac{\partial \eta}{\partial \xi_1}\right), \\ \phi_2 &= \frac{\partial \xi_2}{\partial x_2} - 1 = \frac{\eta}{\delta - \eta}, \\ \phi_3 &= \frac{\partial \xi_2}{\partial x_3} = \frac{1}{\delta - \eta}\left(\xi_2 \frac{\partial \eta}{\partial \xi_3} - \delta \frac{\partial \eta}{\partial \xi_3}\right). \end{aligned}\right\} \tag{2.7}$$

The wave motion is modelled as a potential flow (Liu *et al.* 2010; Yang *et al.* 2014), which can be described by the velocity potential Φ satisfying the Laplace equation:

$$\nabla^2 \Phi = \frac{\partial^2 \Phi}{\partial x^2} + \frac{\partial^2 \Phi}{\partial y^2} + \frac{\partial^2 \Phi}{\partial z^2} = 0. \tag{2.8}$$

https://doi.org/10.1017/jfm.2020.246 Published online by Cambridge University Press

The free-surface kinematic and dynamic conditions are

$$\frac{\partial \eta}{\partial t} + u\frac{\partial \eta}{\partial x} + w\frac{\partial \eta}{\partial z} - v = 0 \quad \text{at } y = \eta, \tag{2.9}$$

$$\frac{\partial \Phi}{\partial t} + gy + \frac{1}{2}(\nabla\Phi \cdot \nabla\Phi) + \frac{P_a}{\rho_w} = 0 \quad \text{at } y = \eta, \tag{2.10}$$

where η is the water surface elevation, P_a is the atmospheric pressure at the surface, ρ_w is the water density and g is the gravitational acceleration. Here and hereinafter, $y = 0$ represents the mean water level and $y = \eta$ represents the instantaneous water surface.

In the HOS method, the velocity potential on the free surface is defined as $\Phi^s = \Phi|_{y=\eta}$ and the velocity potential is expanded as a perturbation series of the velocity potential:

$$\Phi(x, y, z, t) = \sum_{m=1}^{M} \Phi^{(m)}(x, y, z, t), \tag{2.11}$$

where $\Phi^{(m)} = O(\varepsilon^m)$ are the perturbation potentials with ε denoting a measure of the wave steepness.

For each perturbation potential $\Phi^{(m)}$, the Taylor series expansion about the mean water level is expressed as follows:

$$\Phi^s(x, z, t) = \sum_{m=1}^{M} \sum_{l=0}^{M-m} \frac{\eta^l}{l!} \left.\frac{\partial^l \Phi^{(m)}}{\partial y^l}\right|_{y=0}. \tag{2.12}$$

By substituting Φ^s into (2.9) and (2.10), the dimensionless governing equations for the surface elevation and surface potential are given as

$$\frac{\partial \eta}{\partial t} = -\nabla_h\eta \cdot \nabla_h\Phi^s + (1 + \nabla_h\eta \cdot \nabla_h\eta) \times \Phi_y(x, \eta, z, t), \tag{2.13}$$

$$\frac{\partial \Phi^s}{\partial t} = -\frac{1}{Fr^2}\eta - \frac{1}{2}\nabla_h\Phi^s \cdot \nabla_h\Phi^s + \frac{1}{2}(1 + \nabla_h\eta \cdot \nabla_h\eta) \times \Phi_y^2(x, \eta, z, t) - \frac{\rho_a}{\rho_w}P_a(x, z, t), \tag{2.14}$$

where $\nabla_h = (\partial/\partial x, \partial/\partial z)$ is the horizontal gradient operator, ρ_a/ρ_w is the density ratio of air to water and $Fr = U_m/(g\delta)^{1/2}$ is the Froude number. Details of the HOS method can be found in Dommermuth & Yue (1987) and Mei, Stiassnie & Yue (2005).

2.2. *Simulation set-up*

To start the DNS–HOS simulation, the initial airflow field together with the initial wave field need to be specified. Here, the initial airflow is obtained using the DNS data of turbulent flow over a flat wall, and the lower boundary is gradually changed to dynamically evolving surface waves. On the other hand, the initial broadband wave field is generated according to the JONSWAP ocean wave spectrum, which was obtained during the Joint North Sea Wave Project (Hasselmann *et al.* 1973). The directional JONSWAP wave spectrum is expressed as

$$S(\omega, \theta) = \frac{\alpha g^2}{\omega^5} \exp\left[-\frac{5}{4}\left(\frac{\omega}{\omega_p}\right)^{-4}\right] \gamma^{\exp[-((\omega-\omega_p)^2)/(2\sigma^2\omega_p^2)]} D(\theta), \tag{2.15}$$

https://doi.org/10.1017/jfm.2020.246 Published online by Cambridge University Press

where α is the Phillips parameter, γ is the peak enhancement factor, ω is the wave frequency, ω_p is the peak wave frequency and $\sigma = 0.07$ for $\omega \leqslant \omega_p$ and $\sigma = 0.09$ for $\omega > \omega_p$. In (2.10), the directional spreading is given by a cosine-squared function:

$$D(\theta) = \begin{cases} \dfrac{2}{\Theta} \cos^2 \dfrac{\pi\theta}{\Theta}, & |\theta| \leqslant \Theta/2, \\ 0, & |\theta| > \Theta/2, \end{cases} \tag{2.16}$$

where $\theta = \tan^{-1}(k_z/k_x)$ is the wave propagation direction angle, with $k = (k_x, k_z)$ denoting the wavenumber vector, and Θ is the directional spreading width, which is set to π here. According to the results of Liu *et al.* (2010), the wave age has a greater influence on the wind–wave momentum and energy exchange than the wave steepness, and thus the wave age is more important for the investigation of energy transfer in the airflow. Due to the fact that the wave field cannot respond rapidly to changes in the wind field, the local wind speed may vary fast without significant changes in the wave spectrum. Based on this scenario, we define different wave ages based on the peak wave component and the *in situ* wind condition in the present simulations. Two representative dominant wave ages are considered, namely $c_p/u_* = 2$ (slow waves) and 25 (fast waves), and a flat-wall case is also considered for comparison. The flow is driven by a mean pressure gradient to ensure a constant flow rate. The computational parameters are given in table 1.

The free-slip condition is applied at the top boundary, and the bottom boundary condition is provided by the broadband wave motion obtained from the HOS simulation with a 288 × 288 grid. The periodic condition is applied in the streamwise and spanwise directions for both the turbulent flow and wave motions. The computational flow domain has a size of $(L_x, L_y, L_z) = (2\pi\delta, \delta, \pi\delta)$ with a grid number of $(N_x, N_y, N_z) = (192, 144, 192)$. The grid number is nearly the same as that of the DNS of Yang & Shen (2017) and higher than that of Yang & Shen (2010). In particular, uniform grid sizes are used in the streamwise and spanwise directions with $\Delta\xi_1^+ \approx 9.8$ and $\Delta\xi_3^+ \approx 4.9$, respectively, and the vertical grid is stretched from $\Delta\xi_{2,min}^+ \approx 0.018$ in the vicinity of the wavy boundary to $\Delta\xi_{2,max}^+ \approx 3.27$ at the top. All simulations are carried out for about 16 000 viscous time units (tu_*^2/ν), and the turbulence field has reached a statistically stationary state when the data are collected. Statistics are obtained from 300 instantaneous flow field data with an approximate time interval of 20 viscous time units between each dataset.

In the present study, the turbulence–wave simulation uses a one-way coupling scheme. In other words, the effect of overlying turbulence on surface waves is neglected. The surface wave field evolves in time, and the surface elevation and orbital velocities are provided as the bottom boundary conditions for the simulation of the overlying flow at each computational time step. It should be pointed out that two-way coupling is used when considering the wind-forcing effect on the wave field evolution and wave growth rate (Liu *et al.* 2010; Yang *et al.* 2014; Hao & Shen 2019). As pointed out by Hao & Shen (2019), it takes a much longer time of up to $O(3000)$ peak wave periods for the wave spectrum to show appreciable change, as compared with the turbulent flow scales. For a short duration, the one-way and two-way coupling schemes result in only a slight difference in the wave spectrum for the waves at high wavenumbers (Yang & Shen 2011). Compared with the fast-wave-field case, the influence of the airflow on the slow wave field is greater indeed. But overall, the influence of the airflow on the wave field is still a much longer process compared with the much faster eddy-turnover process in the turbulent

https://doi.org/10.1017/jfm.2020.246 Published online by Cambridge University Press

Case	k_p	a^+	c_p/u_*	Re_τ
Flat wall	0	0	0	298
Broadband waves	2	7.3	2	334
	2	6.1	25	285

TABLE 1. Parameters of the computational set-up, including the dimensionless peak wavenumber k_p, the wave amplitude normalized by the wall viscous unit a^+, the wave phase speed normalized by the friction velocity c_p/u_* and the Reynolds number Re_τ based on the friction velocity and channel half-width. For broadband waves, $a=\sqrt{2}a_{rms}$, where a_{rms} denotes the root mean square of wave amplitudes.

airflow above surface waves. The main focus of the present work is the effects of surface waves on the overlying turbulent flow, and consequently the current one-way coupling treatment is adequate for capturing the turbulent flow behaviours under the impact of surface waves (Yang, Meneveau & Shen 2013).

2.3. *Two-point correlation transport equation in curvilinear coordinates*

For inhomogeneous turbulence, the one-point Reynolds stresses transport equation can be employed to describe the turbulent kinetic energy production, dissipation and transport in physical space. However, in order to reveal the scale dependence of the energy transfer process, we resort to the two-point correlation transport equation (Lee & Moser 2015, 2019). In curvilinear coordinates, if we write the equation of velocity fluctuations u_i' (including both the turbulent and wave-coherent components) at one point $(\xi_1, \xi_2, \xi_3, \tau)$, and multiply it by the velocity fluctuations u_{rj}' at another point $(\xi_1+r_{\xi_1}, \xi_2, \xi_3+r_{\xi_3}, \tau)$, adding the ξ_2-plane average of this equation to its counterpart with the subscripts exchanged, we can obtain the transport equation of two-point correlation, i.e.

$$\frac{\partial \overline{u_i'u_{rj}'}}{\partial \tau}(r_{\xi_1}, \xi_2, r_{\xi_3}) = P_{ij} + \Pi_{s,ij} + T_{t,ij} + T_{p,ij} + T_{v,ij} - \varepsilon_{ij} + A_{ij}. \tag{2.17}$$

The right-hand side of (2.17) contains the production, pressure-strain, turbulent transport, pressure transport, viscous transport and dissipation terms, which can be expressed, respectively, as follows:

$$P_{ij} = -(\overline{u_{rj}'v'}\delta_{i1} + \overline{u_i'v_r'}\delta_{j1} + \overline{u_{rj}'u_k'\phi_k}\delta_{i1} + \overline{u_i'u_{rk}'\phi_{rk}}\delta_{j1})\frac{\partial U}{\partial \xi_2}, \tag{2.18}$$

$$\begin{aligned}\Pi_{s,ij} = {} & \frac{\partial \overline{p'u_{rj}'}}{\partial r_{\xi_1}}\delta_{i1} - \frac{\partial \overline{p_r'u_i'}}{\partial r_{\xi_1}}\delta_{j1} + \overline{p'\frac{\partial u_{rj}'}{\partial \xi_2}}\delta_{i2} + \overline{p_r'\frac{\partial u_i'}{\partial \xi_2}}\delta_{j2} \\ & + \frac{\partial \overline{p'u_{rj}'}}{\partial r_{\xi_3}}\delta_{i3} - \frac{\partial \overline{p_r'u_i'}}{\partial r_{\xi_3}}\delta_{j3} + \overline{p'\phi_i\frac{\partial u_{rj}'}{\partial \xi_2}} + \overline{p_r'\phi_{rj}\frac{\partial u_i'}{\partial \xi_2}},\end{aligned} \tag{2.19}$$

$$\begin{aligned}T_{t,ij} = {} & \frac{\partial \overline{u_{rj}'(u_i'u')}}{\partial r_{\xi_1}} - \frac{\partial \overline{u_i'(u_{rj}'u_r')}}{\partial r_{\xi_1}} - \overline{u_{rj}'\frac{\partial u_i'v'}{\partial \xi_2}} - \overline{u_i'\frac{\partial u_{rj}'v_r'}{\partial \xi_2}} \\ & + \frac{\partial \overline{u_{rj}'(u_i'w')}}{\partial r_{\xi_3}} - \frac{\partial \overline{u_i'(u_{rj}'w_r')}}{\partial r_{\xi_3}} - \overline{u_{rj}'\phi_k\frac{\partial u_i'u_k'}{\partial \xi_2}} - \overline{u_i'\phi_{rk}\frac{\partial u_{rj}'u_{rk}'}{\partial \xi_2}},\end{aligned} \tag{2.20}$$

https://doi.org/10.1017/jfm.2020.246 Published online by Cambridge University Press

$$T_{p,ij} = -\overline{\frac{\partial p' u'_{rj}}{\partial \xi_2}}\delta_{i2} - \overline{\frac{\partial p'_r u'_i}{\partial \xi_2}}\delta_{j2} - \overline{\phi_i \frac{\partial p' u'_{rj}}{\partial \xi_2}} - \overline{\phi_{rj} \frac{\partial p'_r u'_i}{\partial \xi_2}}, \tag{2.21}$$

$$T_{v,ij} = \nu \overline{\frac{\partial^2 u'_i u'_{rj}}{\partial \xi_2 \partial \xi_2}} + 2\nu \overline{\phi_2 \frac{\partial}{\partial \xi_2}\left(u'_{rj}\frac{\partial u'_i}{\partial \xi_2}\right)} + 2\nu \overline{\phi_{r2} \frac{\partial}{\partial \xi_2}\left(u'_i \frac{\partial u'_{rj}}{\partial \xi_2}\right)} + \psi_{T_{v,ij}}, \tag{2.22}$$

$$\varepsilon_{ij} = 2\nu \overline{\frac{\partial^2 u'_i u'_{rj}}{\partial r_{\xi_1} \partial r_{\xi_1}}} - 2\nu \overline{\frac{\partial u'_i}{\partial \xi_2}\frac{\partial u'_{rj}}{\partial \xi_2}} + 2\nu \overline{\frac{\partial^2 u'_i u'_{rj}}{\partial r_{\xi_3} \partial r_{\xi_3}}} - 2\nu \overline{(\phi_2 + \phi_{r2})\frac{\partial u'_i}{\partial \xi_2}\frac{\partial u'_{rj}}{\partial \xi_2}} + \psi_{\varepsilon_{ij}}, \tag{2.23}$$

$$\begin{aligned} A_{ij} \;=\; & -(\overline{u'_{rj}\phi_1}\delta_{i1} + \overline{u'_i \phi_{r1}}\delta_{j1})\frac{\partial \bar{u}\bar{u}}{\partial \xi_2} - (\overline{u'_{rj}\phi_i} + \overline{u'_i \phi_{rj}})\frac{\partial \bar{p}}{\partial \xi_2} \\ & + 2\nu(\overline{\phi_2 u'_{rj}}\delta_{i1} + \overline{\phi_{r2} u'_i}\delta_{j1})\frac{\partial^2 \bar{u}}{\partial \xi_2 \partial \xi_2}, \end{aligned} \tag{2.24}$$

where the overbar denotes the ensemble average on a curved plane of the wave-boundary-fitted grid and over time. In addition, it should be noted that the viscous transport and dissipation terms only consider the principal parts here, where ψ_{ij} denotes the viscous cross terms as a result of coordinate transformation and A_{ij} denotes the additional terms due to the effects of boundary deformation on the mean flow. Note that this ensemble average allows us to quantify the statistical properties of the flow in the thin viscous sublayer very close to the wavy surface as has been used in previous studies of turbulent flows over waves (Sullivan *et al.* 2000; Kihara *et al.* 2007; Yang & Shen 2017). If averaging on the Cartesian grid on a horizontal plane is applied, regions below the wave crest cannot be accounted for (see e.g. the discussion in Rutgersson & Sullivan (2005)). We find the difference between the results calculated from these two averaging methods to be small at a short distance above the wave crest and it becomes negligible as the surface-fitted grid becomes flatter at higher elevations.

Furthermore, the turbulent transport term $T_{t,ij}$ can be decomposed into two parts as follows:

$$T_{t,ij} = T^{\alpha}_{t,ij} + T^{\beta}_{t,ij}, \tag{2.25}$$

$$T^{\alpha}_{t,ij} = -\frac{1}{2}\overline{\frac{\partial u'_{rj}(u'_i v')}{\partial \xi_2}} - \frac{1}{2}\overline{\frac{\partial u'_i (u'_{rj} v'_r)}{\partial \xi_2}} - \frac{1}{2}\overline{\phi_k \frac{\partial u'_{rj}(u'_i u'_k)}{\partial \xi_2}} - \frac{1}{2}\overline{\phi_{rk}\frac{\partial u'_i (u'_{rj} u'_{rk})}{\partial \xi_2}}, \tag{2.26}$$

$$\begin{aligned} T^{\beta}_{t,ij} \;=\; & \overline{\frac{\partial u'_{rj}(u'_i u')}{\partial r_{\xi_1}}} - \overline{\frac{\partial u'_i (u'_{rj} u'_r)}{\partial r_{\xi_1}}} + \overline{\frac{\partial u'_{rj}(u'_i w')}{\partial r_{\xi_3}}} - \overline{\frac{\partial u'_i (u'_{rj} w'_r)}{\partial r_{\xi_3}}} \\ & - \frac{1}{2}\overline{\frac{\partial u'_{rj}(u'_i v')}{\partial \xi_2}} - \frac{1}{2}\overline{\frac{\partial u'_i (u'_{rj} v'_r)}{\partial \xi_2}} + \overline{(u'_i v')\frac{\partial u'_{rj}}{\partial \xi_2}} + \overline{(u'_{rj} v'_r)\frac{\partial u'_i}{\partial \xi_2}} \\ & - \frac{1}{2}\overline{\phi_k \frac{\partial u'_{rj}(u'_i u'_k)}{\partial \xi_2}} - \frac{1}{2}\overline{\phi_{rk}\frac{\partial u'_i (u'_{rj} u'_{rk})}{\partial \xi_2}} + \overline{u'_i u'_k \phi_k \frac{\partial u'_{rj}}{\partial \xi_2}} + \overline{u'_{rj} u'_{rk} \phi_{rk}\frac{\partial u'_i}{\partial \xi_2}}, \end{aligned} \tag{2.27}$$

where $T^{\beta}_{t,ij}$ satisfies

$$\lim_{\substack{r_{\xi_1}\to 0 \\ r_{\xi_3}\to 0}} T^{\beta}_{t,ij} = 0, \quad \forall \xi_2. \tag{2.28}$$

Therefore, $T^{\beta}_{t,ij}$ can be interpreted as the inter-scale energy transfer and does not contribute to the net spatial energy flux (see appendix A). Hereafter, $T^{\beta}_{t,ij}$ is referred

https://doi.org/10.1017/jfm.2020.246 Published online by Cambridge University Press

to as the inter-scale turbulent transport and $T^{\alpha}_{t,ij}$ is called the spatial turbulent transport. Note that the nonlinear term decomposition is not unique. The present spatial and inter-scale parts depicted in (2.26) and (2.27) are consistent with the decomposition adopted by Mizuno (2016) and Lee & Moser (2019) for flat-wall turbulence. It should be noted that although the energy transfer between vertical scales is also important for understanding wall-bounded turbulence, it is beyond the scope of the present work. It may be better to investigate the energy distribution on vertical scales based on the generalized Kolmogorov equation, as recently studied by Cimarelli *et al.* (2016).

By performing a Fourier transform in the ξ_1 and ξ_3 directions, equation (2.17) becomes

$$\frac{\partial \hat{E}_{ij}}{\partial \tau}(k_{\xi_1}, \xi_2, k_{\xi_3}) = \hat{E}^{P}_{ij} + \hat{E}^{\Pi_s}_{ij} + \hat{E}^{T^{\alpha}_t}_{ij} + \hat{E}^{T^{\beta}_t}_{ij} + \hat{E}^{T_p}_{ij} + \hat{E}^{T_v}_{ij} - \hat{E}^{\varepsilon}_{ij} + \hat{E}^{A}_{ij}, \tag{2.29}$$

where each term is the Fourier transform of its counterpart in (2.17). The one-dimensional energy spectrum is defined as

$$E_{ij}(k_{\xi_1}, \xi_2) = \sum_{k_{\xi_3}} [\hat{E}_{ij}(k_{\xi_1}, \xi_2, k_{\xi_3}) + \hat{E}_{ij}(-k_{\xi_1}, \xi_2, k_{\xi_3})] \tag{2.30}$$

or

$$E_{ij}(k_{\xi_3}, \xi_2) = \sum_{k_{\xi_1}} [\hat{E}_{ij}(k_{\xi_1}, \xi_2, k_{\xi_3}) + \hat{E}_{ij}(k_{\xi_1}, \xi_2, -k_{\xi_3})], \tag{2.31}$$

and similarly for the other terms. Then, the transport equation of the one-dimensional energy spectrum E_{ij} is obtained as

$$\frac{\partial E_{ij}}{\partial \tau} = E_{p,ij} + E_{\Pi_s,ij} + E_{T^{\alpha}_t,ij} + E_{T^{\beta}_t,ij} + E_{T_p,ij} + E_{T_v,ij} - E_{\varepsilon,ij} + E_{A,ij}. \tag{2.32}$$

Further analysis of the terms in (2.32) is presented in § 3, which describes the processes of how energy is produced, dissipated and transported among different scales and locations, and provides a general turbulent energy transfer framework in the presence of surface waves. Note that E_{ij} is a function of ξ_2, which represents the mean vertical distance away from the wave surface, i.e. $\bar{y} = \xi_2$. In the following, we omit the overbar and use y to indicate the vertical distance without special note for brevity. The streamwise and spanwise wavenumbers are denoted by k_1 and k_3, respectively, in the computational domain, and λ_1 and λ_3 are the corresponding streamwise and spanwise wavelengths.

3. Results and discussion

3.1. *Flow visualization*

Before discussing the turbulence statistics, it is instructive to examine the instantaneous turbulence field over water waves from visualization of the data generated by the DNS–HOS simulation. Taking the slow-wave case of $c_p/u_* = 2$ as an example, figure 2 shows the three-dimensional instantaneous flow field. The distribution of the turbulent flow pressure on the wave surface is closely related to the surface slope with generally positive (negative) values on the windward (leeward) side. The overlying vortical structures are visualized via the isosurface of the local swirling strength λ_{ci} (Zhou *et al.* 1999). As shown in the figure, they are dominated by the

https://doi.org/10.1017/jfm.2020.246 Published online by Cambridge University Press

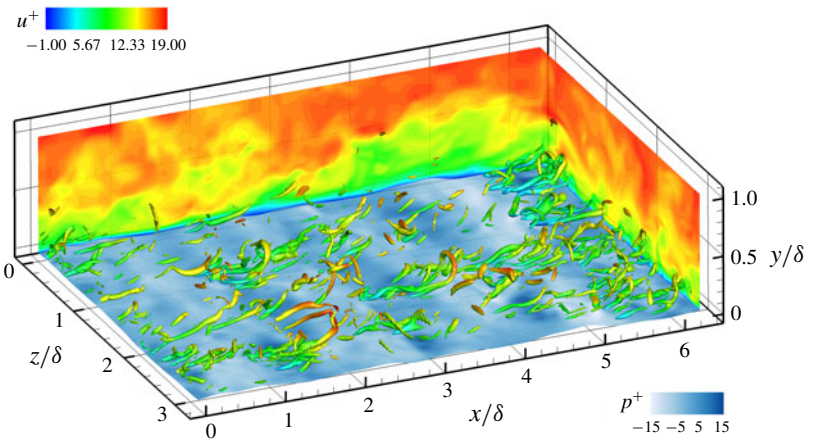


FIGURE 2. Illustration of the three-dimensional flow field over surface waves for the case of $c_p/u_* = 2$. Contours of the instantaneous streamwise velocity are plotted in the x–y plane and the y–z plane. The distribution of the turbulent flow pressure on the wave surface is also shown. The vortical structures are identified by the isosurface of 10 % of the maximum λ_{ci} and coloured by the instantaneous streamwise velocity.

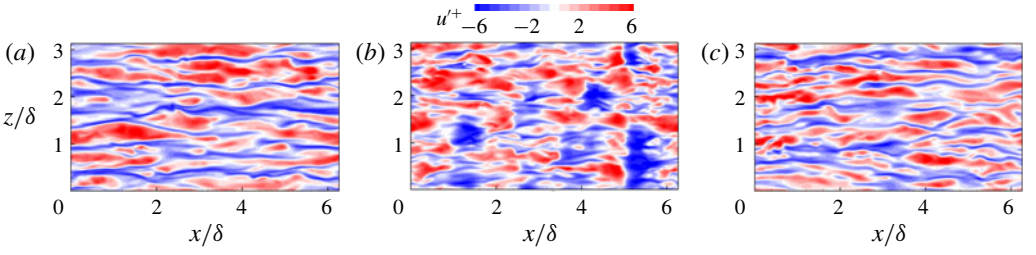


FIGURE 3. Instantaneous streamwise velocity fluctuation in the x–z plane located at $y^+ = 12$: (*a*) the flat-wall case; (*b*) $c_p/u_* = 2$; (*c*) $c_p/u_* = 25$.

quasi-streamwise vortices and affected by the surface waves. The streamwise size of these vortices is constrained by the dominant wavelength and the inclination angle is modulated by the waveform, as suggested by Yang & Shen (2009). The contours of the streamwise velocity in the x–y plane are tilted downstream in the near-surface region, consistent with the posture of the streamwise vortices. Note that the low-speed zones are lifted up in the y–z plane, corresponding to the formation of streaky structures.

Figure 3 shows the instantaneous contours of the streamwise velocity fluctuations in the x–z plane located at $y^+ = 12$. For the flat-wall case, the flow pattern in figure 3(*a*) is dominated by the streamwise elongated low-speed streaks. In the presence of the surface waves, the typical flat-wall streaky structures are disrupted by the periodic wave motions. As shown in figure 3(*b*), the velocity fluctuation alternates in sign in the streamwise direction with the spatial periodicity corresponding to the dominant wavelength λ_p. As the wave age increases to $c_p/u_* = 25$, the effect of the surface waves on the flow structure is greatly attenuated, and the streaky structures similar to the flat-wall turbulence case (figure 3*a*) are recovered in figure 3(*c*). These results

https://doi.org/10.1017/jfm.2020.246 Published online by Cambridge University Press

show clearly the impact of surface waves on the turbulent flow field above. The effects on turbulent energy are analysed in detail in the following subsections.

3.2. *Energy spectra*

The main objective of the present study is to explore the turbulent energy transfer process under the impact of surface waves. We begin by examining the energy distribution at different length scales and vertical locations. The one-dimensional premultiplied energy spectra of the streamwise velocity fluctuations on the plane of the streamwise wavelength λ_1 (or the spanwise wavelength λ_3) and y are plotted in figure 4. For the flat-wall case, the spectral peaks in figures 4(*a*) and 4(*d*) are consistent with the results of Marusic, Mathis & Hutchins (2010) and Smits, McKeon & Marusic (2011). The peaks denote the streamwise length ($\lambda_1^+ \approx 1000$) and the spanwise spacing ($\lambda_3^+ \approx 100$) of the low-speed streaky structures in the buffer region (see figure 3*a*), which are important elements of the near-wall self-sustaining process as described by Hamilton, Kim & Waleffe (1995) and Jiménez & Pinelli (1999). For the slow-wave-field case of $c_p/u_* = 2$, as seen in figure 4(*b*), the streamwise length scale of the peak in the buffer region becomes the wavelength of dominant surface wave, $\lambda_p^+ \approx 524.8$. In addition, energy is also concentrated at the harmonic wavelengths (figure 4*b*), significantly different from the flat-wall case. In other words, the original low-speed streaky structures are disrupted by the surface waves, as seen in figure 3(*b*) and previously observed by Sullivan *et al.* (2000). As the wave age increases to $c_p/u_* = 25$ (figure 4*c*), in the fast-wave-field case, the streamwise energy spectrum protrudes from the wavy boundary over a range of scales, centring around the dominant wavelength, which can be attributed to the direct contribution of the surface waves to the streamwise Reynolds stress. In the buffer region, the peak position still occurs at the dominant wavelength scale, but its energy amplitude is much smaller than that in the slow-wave case shown in figure 4(*b*). This result indicates that the streaky structures are not obviously altered by the surface waves when the wave age is large, consistent with figure 3(*c*). Furthermore, the one-dimensional spanwise premultiplied energy spectra of the streamwise velocity fluctuations are compared in figure 4(*d–f*). For the case of $c_p/u_* = 2$, a tip of the spanwise energy spectrum occurs at $\lambda_3^+ \approx 500$ in the region of $y^+ \approx 100$ as seen in figure 4(*e*), indicating that the large-scale motion is enhanced by the slow wave. Similar effects of a stationary wavy boundary on the large-scale structures in a turbulent flow were observed in the experimental study by Kuhn, Wagner & von Rohr (2007). As the wave age increases to $c_p/u_* = 25$ (figure 4*f*), the large-scale outer peak is weakened, while an additional local peak region at the surface is observed. The large-scale motions in the very-near-surface region as seen in figure 4(*f*) correspond to the dynamically evolving surface waves, whose dominant component extends to the whole domain in the spanwise direction. After multiplying the spanwise energy spectra by the spanwise wavenumber k_3, a large-scale spectral peak occurs near the surface.

As discussed above, the surface waves have significant influence on the distribution of the turbulent kinetic energy in both physical and spectral spaces. In the following subsections, the premultiplied one-dimensional spectra of the different terms in (2.32) are examined to further explore the underlying mechanism of how surface waves affect the overlying turbulent flow at different length scales and vertical positions.

3.3. *Energy production*

Figure 5 shows the premultiplied one-dimensional streamwise and spanwise spectra of the production term $E_{p,11}$ of the two-point correlation $\overline{u'u'_r}$ in (2.32). For the flat-wall

https://doi.org/10.1017/jfm.2020.246 Published online by Cambridge University Press

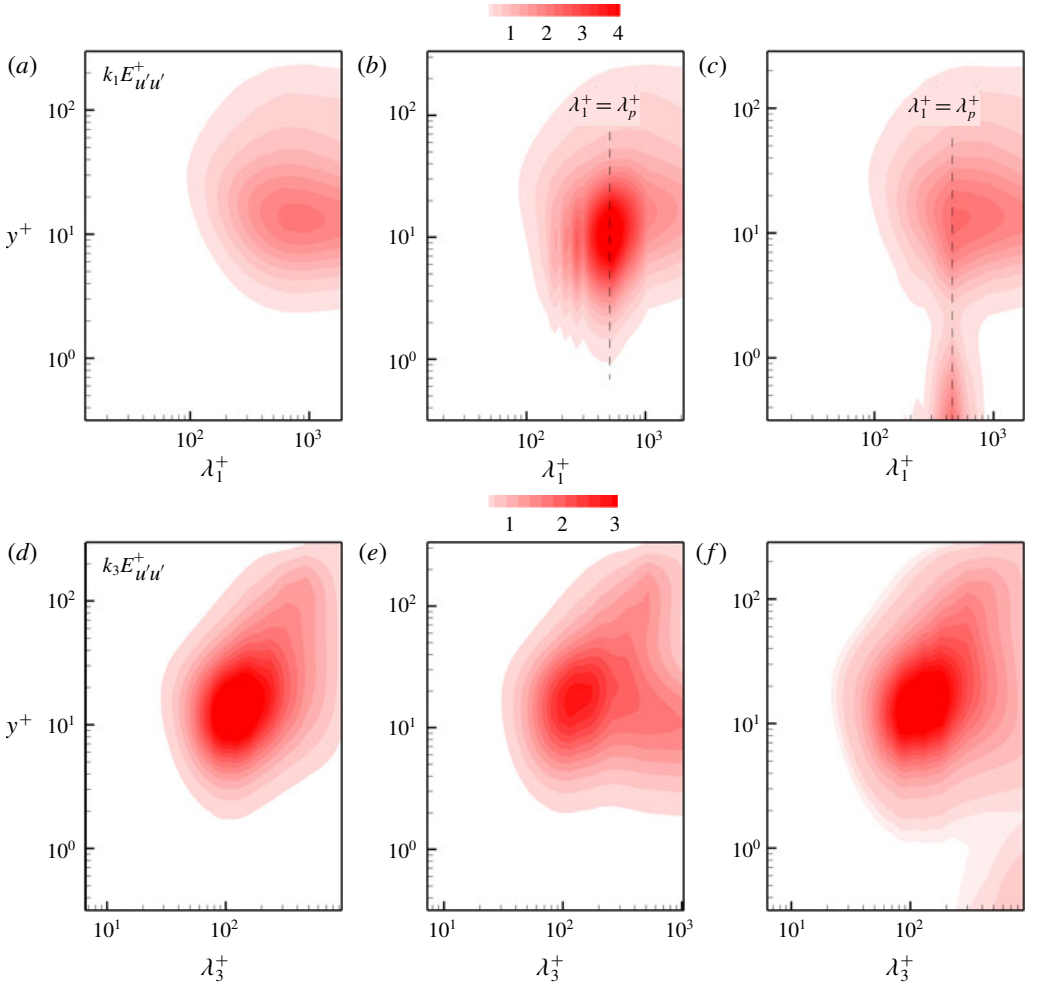


FIGURE 4. One-dimensional streamwise (*a–c*) and spanwise (*d–f*) premultiplied energy spectra of the streamwise velocity fluctuations: (*a*,*d*) the flat-wall case; (*b*,*e*) $c_p/u_* = 2$; (*c*,*f*) $c_p/u_* = 25$.

case, as seen in figures 5(*a*) and 5(*b*), there is a peak in the buffer region with the streamwise and spanwise length scales corresponding to the typical near-wall streaks. Turbulence is most active in the peak region and the turbulent fluctuations gain energy from the mean shear flow. In addition to the positive production at most length scales and vertical locations, it should be noted that there is a small region where the streamwise spectrum of the production term is negative near $y^+ \approx 20$ and $\lambda_1^+ \approx 73.6$ in figure 5(*a*), while no negative region appears in the spanwise spectrum as shown in figure 5(*b*). This weak negative region is related to the positive co-spectrum of $\overline{u'v'}$, as observed in Lee & Moser (2015, 2019) at a higher Reynolds number $Re_\tau = 5200$.

In the presence of the progressive surface waves, the production term $E_{p,11}$ retains the main characteristics of the flat-wall case above the buffer region. However, there are significant differences in the region of $y^+ < 20$. For the case of $c_p/u_* = 2$, as seen in figure 5(*c*), a series of negative spectral peaks appear in the buffer region,

https://doi.org/10.1017/jfm.2020.246 Published online by Cambridge University Press

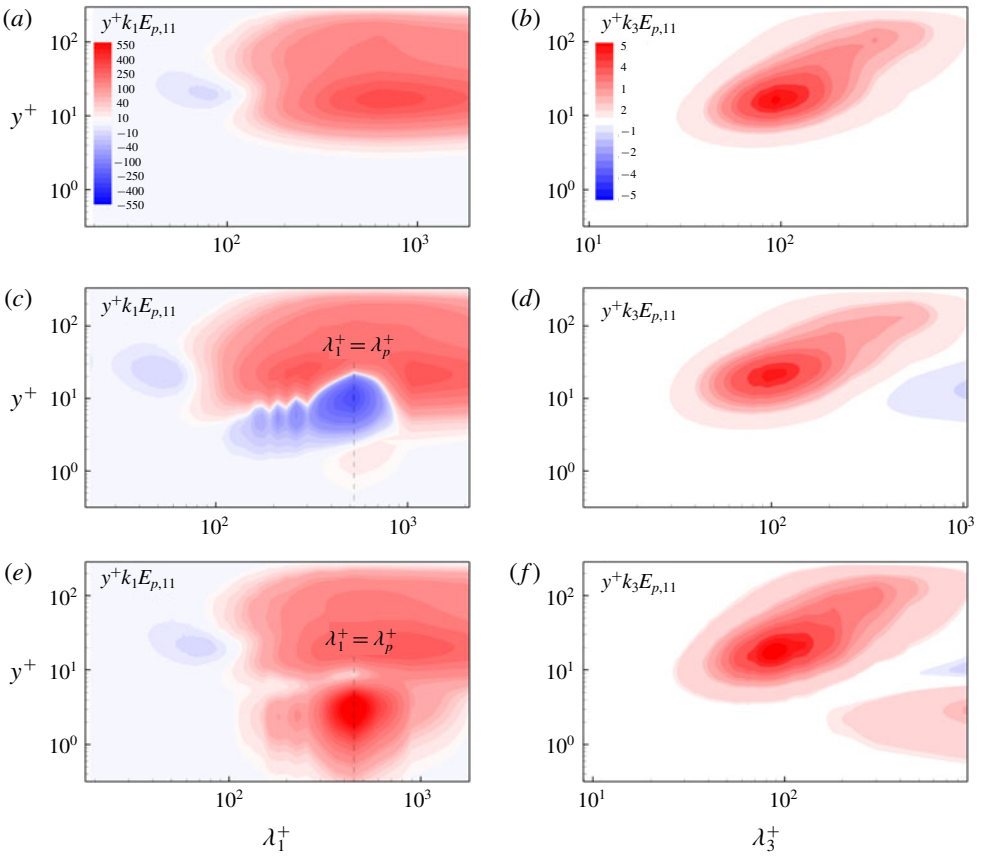


FIGURE 5. The y- and k-premultiplied one-dimensional streamwise (a,c,e) and spanwise (b,d,f) spectra of $E_{p,11}$: (a,b) the flat-wall case; (c,d) $c_p/u_* = 2$; (e,f) $c_p/u_* = 25$.

corresponding to the length scales of the dominant wave and its harmonic waves. In this case, the motions associated with the surface waves act as energy sinks, extracting energy from the fluctuating field to the mean flow. A quadrant analysis indicates that in the presence of surface waves (results not shown here), the contribution from the Q1 and Q3 events is increased significantly in the near-surface region of $y^+ < 10$ due to the wave-induced motions, as compared with the flat-wall case, corresponding to the negative region near the dominant wavelength in figure 5(c). Similarly, the spanwise spectrum shown in figure 5(d) has a large-scale negative region in the region of $y^+ \approx 10$, with the large spanwise length scale reflecting the quasi-two-dimensional characteristics of the broadband wave field. When the wave age increases to $c_p/u_* = 25$, the streamwise spectrum of the production term plotted in figure 5(e) shows a positive region at the dominant wavelength scale in the region of $y^+ < 10$, and contributions of its harmonics to the energy production also emerge. In addition, a positive region near the surface is also observed in figure 5(f), indicating the effect of the wave-induced vertical momentum flux, based on the definition of the production term (2.18) and as further analysed below. It becomes negative at large spanwise length scale similar to the slow-wave case (figure 5d) with an increase of height.

https://doi.org/10.1017/jfm.2020.246 Published online by Cambridge University Press

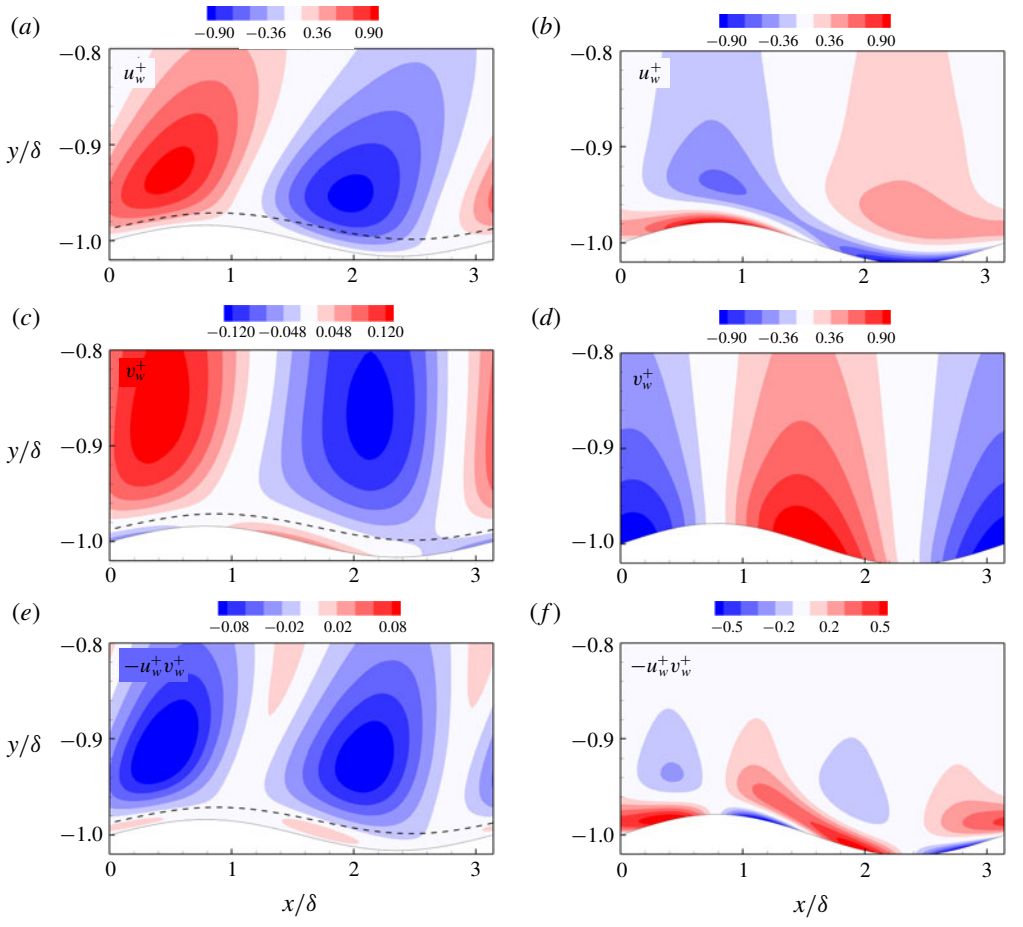


FIGURE 6. Dominant wave-induced streamwise (*a*,*b*) and vertical (*c*,*d*) velocity fluctuations, and vertical momentum flux (*e*,*f*): (*a*,*c*,*e*) $c_p/u_* = 2$; (*b*,*d*,*f*) $c_p/u_* = 25$. The dashed line in (*a*,*c*,*e*) denotes the critical layer.

To explain the change of the streamwise spectrum of the production term at the dominant wavelength scale for the different wave age cases shown above, the wave-coherent and turbulent velocities are decomposed to investigate the wave–turbulence interactions (Thais & Magnaudet 1996; Siddiqui & Loewen 2007). Here, the phase-average approach (Hussain & Reynolds 1970) based on the dominant wavelength is used to perform further analysis. For this purpose, the dominant wave mode is extracted from the instantaneous wave field, and then the corresponding surface deformation and phase information of the dominant wave are obtained. The phase-averaged velocity $\langle \boldsymbol{u} \rangle$ is obtained based on three steps of averaging. First, the velocity is averaged over time in the frame moving with the dominant wave such that its wave phase is fixed. Then the velocity is averaged in the spanwise direction. Finally, the velocity is averaged over all of the dominant waves in the streamwise direction. Based on the phase-averaged velocity $\langle \boldsymbol{u} \rangle$, we define the dominant wave-induced velocity fluctuation $\boldsymbol{u}_w$ as the fluctuation of $\langle \boldsymbol{u} \rangle$ relative to the ensemble average $\bar{\boldsymbol{u}}$, i.e. $\boldsymbol{u}_w = \langle \boldsymbol{u} \rangle - \bar{\boldsymbol{u}}$. The dominant wave-induced velocity fluctuation (u_w, v_w) and the dominant wave-induced vertical momentum flux, $-u_w v_w$, are plotted in figure 6. The critical layer, where $\langle u \rangle = c_p$, has been found to be

https://doi.org/10.1017/jfm.2020.246 Published online by Cambridge University Press

important to the wave-induced motions in field observations (Hristov *et al.* 2003; Grare *et al.* 2013) and is marked in figure 6(*a*,*c*,*e*). For the case of $c_p/u_* = 2$, the dominant wave-induced streamwise velocity fluctuation u_w (figure 6*a*) is positive on the windward side and negative on the leeward side, while the vertical velocity fluctuation v_w (figure 6*c*) on the surface has the opposite distribution, in accordance with the airflow measurements in the laboratory (Buckley & Veron 2016, 2019). Consequently, the dominant wave-induced vertical momentum flux is positive below the critical layer height $y^+ \approx 2.5$ (figure 6*e*), which agrees with the result of Sullivan *et al.* (2000) in their study of monochromatic waves, and has a positive contribution to the production term (2.18). Although the result in figure 18 of Sullivan *et al.* (2000) corresponds to a wave age of $c_p/u_* = 3.9$, slightly larger than the present slow-wave age $c_p/u_* = 2$, the wave-correlated momentum flux across the critical layer is quite similar to that observed in the present study. As the vertical distance from the surface increases, v_w has an abrupt phase shift across the critical layer, with a positive peak above the crest and a negative peak above the trough. As a result of this phase change, the momentum flux changes its sign in the vertical direction and has a large negative value at the dominant wavelength scale (figure 6*e*). As the wave age increases to $c_p/u_* = 25$, the critical layer moves far away from the surface (beyond the vertical extent of the computational domain) and has negligible influence on the wave-induced velocity fluctuations near the surface. As shown in figure 6(*b*), the distribution of u_w is tilted with its negative peak moving from the trough region to the crest due to the rapid propagation of surface waves, while the distribution of v_w remains largely unchanged as the vertical height increases (figure 6*d*). As a result, positive vertical momentum flux exists in most of the near-surface region and it changes its sign as y increases (figure 6*f*). Therefore, the contribution of the surface waves to energy production varies with the distance away from the surface for different wave ages through the wave-induced vertical momentum flux, according to the definition of the production term (2.18).

3.4. *Inter-component energy transfer*

Due to the incompressibility of the flow field, the spectra of the pressure-strain terms of the different velocity components satisfy

$$\hat{E}_{\Pi_s,11} + \hat{E}_{\Pi_s,22} + \hat{E}_{\Pi_s,33} = 0 \quad \forall(k_1, \xi_2, k_3), \tag{3.1}$$

which indicates the energy transfer among different velocity components. For the flat-wall case, the one-dimensional premultiplied spectra of the pressure-strain terms are shown in figure 7. In general, the energy is transferred from the streamwise velocity component to the vertical and spanwise velocity components at $y^+ > 10$. Figure 7(*c*–*f*) shows that at $y^+ < 10$, the energy near the peak region of $\lambda_1^+ = 305.3$ and $\lambda_3^+ = 93.6$ is transferred from the vertical component to the spanwise component, which is consistent with the result of Lee & Moser (2015). In addition, figure 7(*f*) shows that the energy of the spanwise component near $\lambda_3^+ = 37.3$ is transferred to the vertical component at $y^+ \approx 21.4$. This can be understood in terms of the cross-sectional flow induced by the streamwise vortices, which leads to the preferential transfer of energy into the vertical velocity fluctuations.

Figure 8 shows the streamwise and spanwise spectra of the pressure-strain terms for the slow-wave-field case $c_p/u_* = 2$. It is seen that the spectra of the pressure-strain terms are significantly affected by the surface waves. As plotted in figure 8(*a*,*b*),

https://doi.org/10.1017/jfm.2020.246 Published online by Cambridge University Press

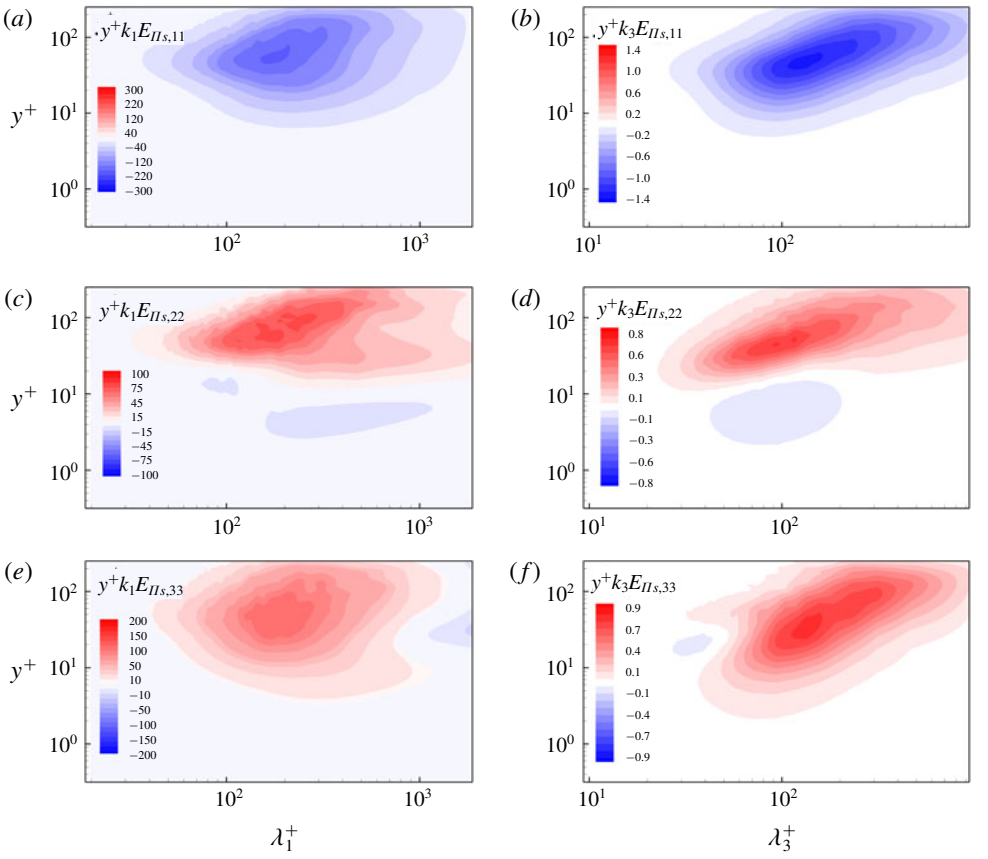


FIGURE 7. The y- and k-premultiplied one-dimensional streamwise (a,c,e) and spanwise (b,d,f) spectra of the pressure-strain terms of different velocity components for the flat-wall case: (a,b) $E_{\Pi_s,11}$; (c,d) $E_{\Pi_s,22}$; (e,f) $E_{\Pi_s,33}$.

the energy is transferred from the streamwise component to the vertical component at the dominant wavelength scale in the region of $y^+ < 10$. Also, the streamwise component has a negative spanwise large-scale peak in figure 8(b), and the vertical component in figure 8(d) has a corresponding positive region. Moreover, it is noted that there is a small negative region at the dominant wavelength scale near $y^+ \approx 15$ in figure 8(c), which is explained below. Moreover, the spanwise component shown in figures 8(e) and 8(f) is similar to that of the flat-wall case (figures 7e and 7f). It is noted that the spectral peak in the region of $y^+ < 10$ in figure 8(e) is around the dominant wavelength, although not as obvious as those in figures 8(a) and 8(c). Due to the fact that the surface waves contribute to the total energy mainly through the vertical momentum flux $-u'v'$, the energy transfer between streamwise and vertical components dominates the inter-component energy transfer. Therefore, the peaks in the spectra of the spanwise component (figure 8e,f) are much weaker and similar to those in the flat-wall case (figure 7e,f), especially in the spanwise spectra (figure 8f).

For the fast-wave-field case $c_p/u_* = 25$, the streamwise and spanwise spectra of the pressure-strain terms in figure 9 show apparent differences compared with the slow-wave-field case $c_p/u_* = 2$ plotted in figure 8. As seen in figures 9(c) and 9(d), energy is transferred from the vertical velocity component to the other two

https://doi.org/10.1017/jfm.2020.246 Published online by Cambridge University Press

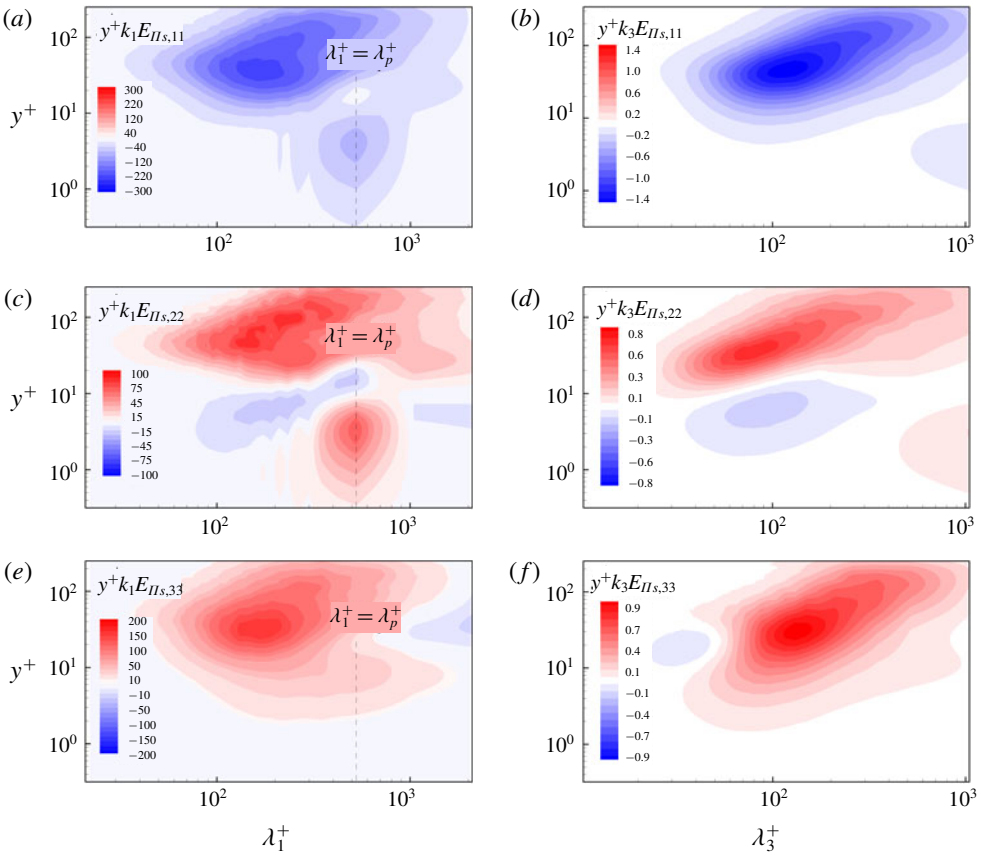


FIGURE 8. The y- and k-premultiplied one-dimensional streamwise (a,c,e) and spanwise (b,d,f) spectra of the pressure-strain terms of different velocity components for the case of $c_p/u_* = 2$: (a,b) $E_{\Pi_s,11}$; (c,d) $E_{\Pi_s,22}$; (e,f) $E_{\Pi_s,33}$.

velocity components at the dominant wavelength scale for $y^+ < 10$. Correspondingly, figure 9(a,b,e,f) has a positive region representing energy gain from the vertical component. The energy transfer direction among the three velocity components is opposite to the case of $c_p/u_* = 2$, which is consistent with the variation of the form drag with the wave age (Sullivan *et al.* 2000; Shen *et al.* 2003; Yang & Shen 2010). With the wave age increasing, the form drag changes from positive to negative and acts as a thrust force, which works positively on the turbulent flow. In other words, the energy is transferred from the surface waves to the overlying airflow mainly through the vertical velocity component. Subsequently, energy is transferred outwards from the vertical velocity component via the pressure-strain terms in the vicinity of the wave surface.

To explain the variation of $E_{\Pi_s,22}$ along the y direction at the dominant wavelength scale (figures 8c and 9c), we plot the dominant wave-induced pressure and velocity gradient fluctuations in figure 10. For the slow-wave case $c_p/u_* = 2$ (figure 10a), the wave-induced pressure is in general positive on the windward side and negative on the leeward side. However, the positive (negative) region of the velocity gradient fluctuation is inclined from the windward (leeward) side to the leeward (windward) side as y increases, as seen in figure 10(b). Since the pressure-strain terms represent

https://doi.org/10.1017/jfm.2020.246 Published online by Cambridge University Press

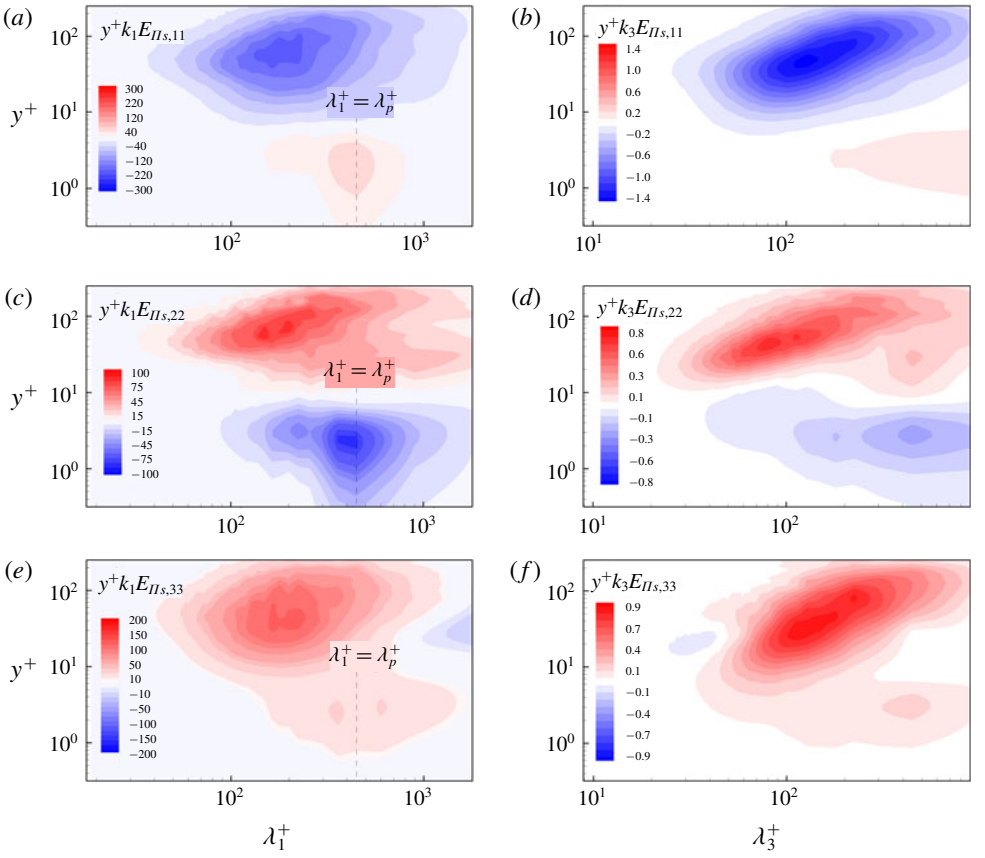


FIGURE 9. The y- and k-premultiplied one-dimensional streamwise (a,c,e) and spanwise (b,d,f) spectra of the pressure-strain terms of different velocity components for the case of $c_p/u_* = 25$: (a,b) $E_{\Pi_s,11}$; (c,d) $E_{\Pi_s,22}$; (e,f) $E_{\Pi_s,33}$.

the combined effect of pressure and velocity gradients (2.19), $E_{\Pi_s,22}$ at the dominant wavelength scale changes its sign from positive to negative at $y^+ = 10$ in figure 8(c). On the other hand, for the fast-wave case $c_p/u_* = 25$, due to the rapid propagation of the surface waves, the negative and positive peaks of the velocity gradient fluctuation are twisted significantly to the upstream direction as y increases (figure 10d). The wave-induced pressure is positive (negative) above the trough (crest) and varies only slightly in the y direction. As a result, the variation of $E_{\Pi_s,22}$ in the y direction of the $c_p/u_* = 25$ case (figure 9c) is opposite to that of $c_p/u_* = 2$ (figure 8c).

The pressure-strain term E_{Π_s} is closely related to the net energy transfer from the wind to the surface waves. We further examine the wave growth rate based on the present simulations and compare the results with the growth rate values predicted from rapid distortion theory (Belcher & Hunt 1993) and measurement data (Mastenbroek *et al.* 1996; Grare *et al.* 2013) as well as numerical data (Sullivan *et al.* 2000; Liu *et al.* 2010; Yang & Shen 2010). Here we extract the dominant wave mode and the corresponding pressure at the surface to compute the wave growth rate β following Liu *et al.* (2010). Suppose the dominant wave component of the surface elevation is $\eta(x,\ t) = a\ \cos(k_p x - \omega_p t)$ and the corresponding surface pressure is $p(x,\ t) = \alpha ak\cos(k_p x - \omega_p t + \theta)$, where α denotes the amplitude ratio of the pressure

https://doi.org/10.1017/jfm.2020.246 Published online by Cambridge University Press

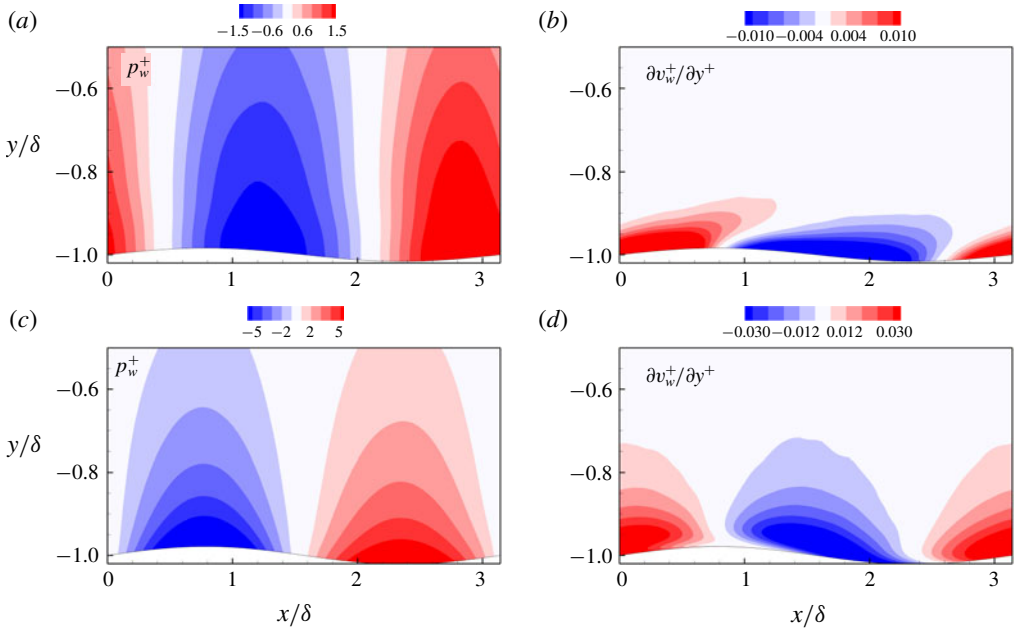


FIGURE 10. Dominant wave-induced pressure (*a*,*c*) and velocity gradient (*b*,*d*) fluctuations: (*a*,*b*) $c_p/u_* = 2$; (*c*,*d*) $c_p/u_* = 25$.

to the wave steepness and θ denotes the phase difference between the pressure and the waveform. The wave growth rate is then obtained as: $\beta = (\alpha \sin\theta)/\rho u_*^2$. In general, the results are consistent. For the slow-wave-field case, the current result is close to the measurements completed in wave tanks (Mastenbroek *et al.* 1996; Grare *et al.* 2013) as shown in figure 11, which are larger than the theoretical predictions obtained by Belcher & Hunt (1993). Note that the wave steepness also affects the wave growth rate. Therefore, even when the wave age is fixed, there is a noticeable scattering in the wave growth rates calculated in different experimental and numerical studies (e.g. see the data near $c/u_* = 2$ in figure 11).

The above results of energy transfer among different velocity components are summarized as follows. For flat-wall turbulence, the energy is transferred from the streamwise component to the other two components via the pressure-strain terms in the region of $y^+ > 10$. In the presence of surface waves, additional inter-component energy transfer occurs at the dominant wavelength scale in the near-surface region. For the slow-wave case $c_p/u_* = 2$, the inter-component energy transfer direction at the dominant wavelength scale at $y^+ < 10$ is consistent with the main transfer direction in flat-wall turbulence. On the contrary, the energy at the dominant wavelength scale is transferred from the vertical component to the other two components at $y^+ < 10$ for the fast-wave case $c_p/u_* = 25$.

3.5. *Spatial energy transport*

In the region where the energy production from the mean shear is high, the energy is transported vertically to the regions above and below it. As discussed in § 2.3, there are three mechanisms in the spatial energy transport process, namely the viscous transport $T_{v,ij}$, the pressure transport $T_{p,ij}$ and the spatial turbulent transport $T_{t,ij}^{\alpha}$.

https://doi.org/10.1017/jfm.2020.246 Published online by Cambridge University Press

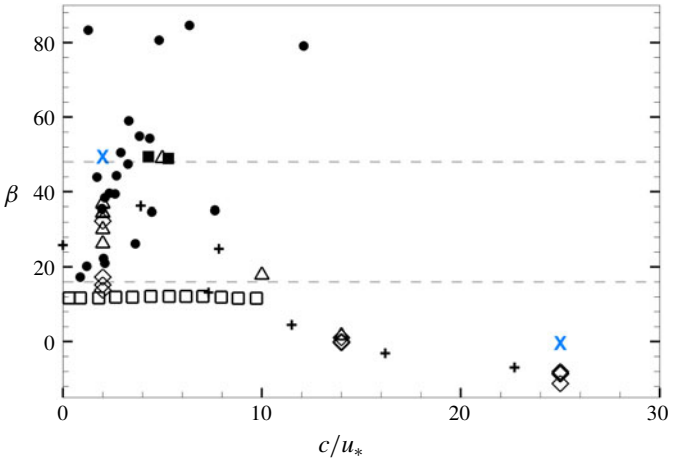


FIGURE 11. Wave growth rate β as a function of wave age c/u_*. Wave tank measurement data are denoted by: ■, Mastenbroek *et al.* (1996); ●, Grare *et al.* (2013). Previous numerical results are denoted by: +, Sullivan *et al.* (2000); △, Liu *et al.* (2010); ◇, Yang & Shen (2010). Also plotted are the upper ($\beta = 48$) and lower ($\beta = 16$) limits of the observation-based empirical formula of Plant (1982), denoted by the horizontal dashed lines. The wave growth rates obtained with the analytical theory of Belcher & Hunt (1993) are denoted by □. Present simulation results are denoted by ×.

The premultiplied one-dimensional streamwise spectra of the turbulent kinetic energy spatial transport terms are plotted in figure 12. In general, the effect of the viscous transport is confined to the region of $y^+ < 70$. For the flat-wall case, it is seen in figure 12(*a*) that energy is transferred from the buffer region to the very-near-wall region and the outer region through the viscous transport. The negative peak in figure 12(*a*) is close to the positive peak of the production term in figure 5(*a*), where the turbulent energy is the highest and is thus transferred to other regions. For the case of $c_p/u_* = 2$, the energy transfer is also from the buffer region to the near-surface and outer regions except that the streamwise length scale of the peak region changes to the dominant wavelength (figure 12*d*). As the wave age increases to $c_p/u_* = 25$, the energy transfer to the very-near-surface region via the viscous transport (red region) increases and occurs at the dominant wavelength scale (figure 12*g*).

As for the turbulent kinetic energy pressure transport, it contributes the least to the spatial energy flux in the flat-wall case as compared with the other two energy transport terms. As shown in figure 12(*b*), the energy transport direction is consistent with the viscous term, but its effect does not reach the surface. In the presence of surface waves, the direction of the pressure transport is strongly dependent on the wave age. For the case of $c_p/u_* = 2$, the energy is transferred from the very-near-surface region to the buffer region at the dominant wavelength scale as seen in figure 12(*e*), while the energy is transferred from the buffer region to the very-near-surface region in the case of $c_p/u_* = 25$ (figure 12*h*). The opposite direction of the turbulent energy transport by pressure can also be explained by the difference in the form drag at different wave ages. As shown in Sullivan *et al.* (2000) and Yang & Shen (2010), the air pressure distribution near the wall is significantly affected by the wave age. When the wave age increases to the fast-wave range, the form drag becomes negative and acts as a thrust, leading to a significant difference in the pressure–velocity correlation.

https://doi.org/10.1017/jfm.2020.246 Published online by Cambridge University Press

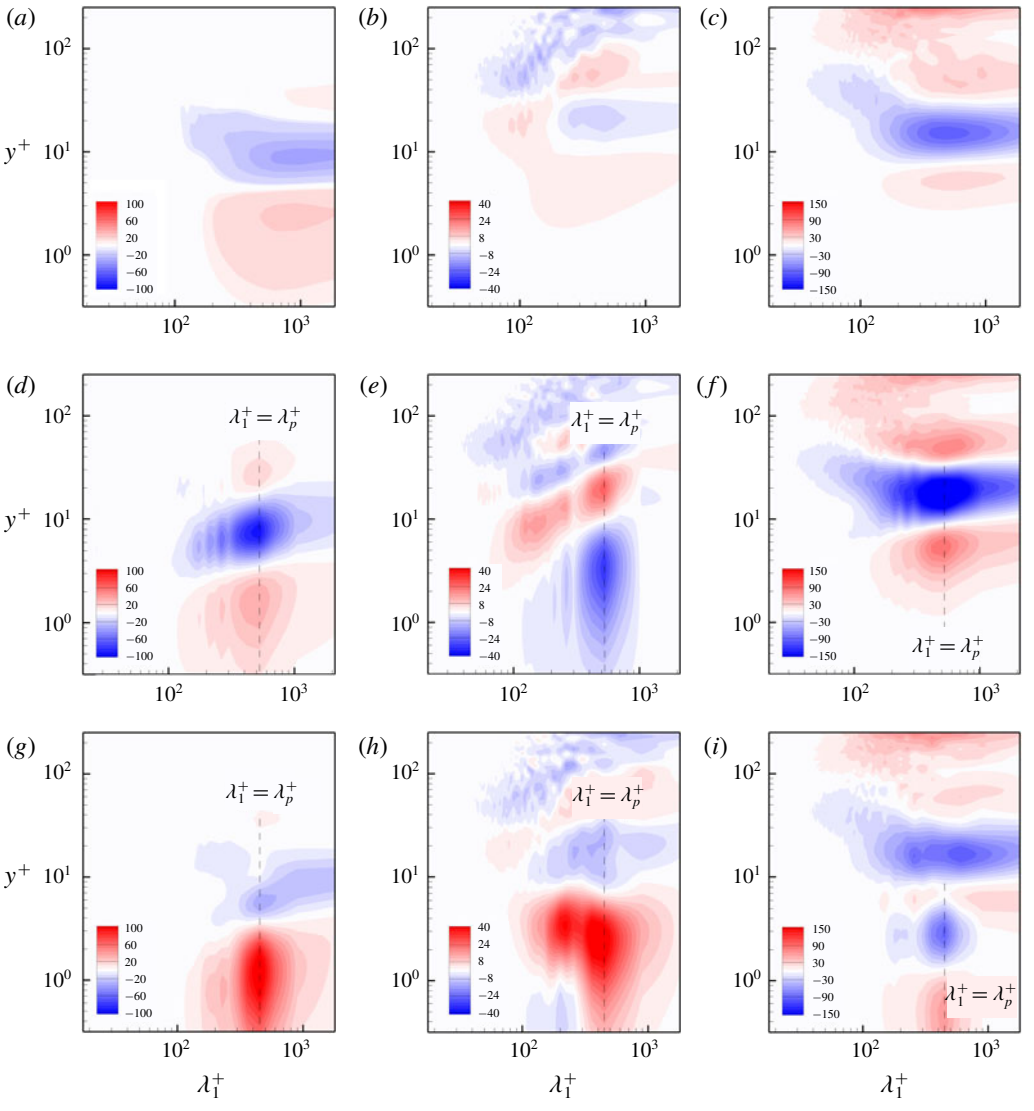


FIGURE 12. The y- and k-premultiplied one-dimensional streamwise spectra of the turbulent kinetic energy: (*a*,*d*,*g*) viscous transport, (*b*,*e*,*h*) pressure transport and (*c*,*f*,*i*) spatial turbulent transport, in the cases of (*a–c*) flat wall; (*d–f*) $c_p/u_* = 2$; (*g–i*) $c_p/u_* = 25$.

After decomposing $T_{t,ij}$ into $T_{t,ij}^{\alpha}$ and $T_{t,ij}^{\beta}$ as in (2.25), the spectrum of $T_{t,ij}^{\alpha}$ can be interpreted as the spatial turbulent transport in the vertical direction. For the flat-wall case, this term contributes the most to the total energy spatial transport as shown in figure 12(*c*). Moreover, the spatial turbulent transport can affect higher locations as compared with the viscous transport in figure 12(*a*). For the case of $c_p/u_* = 2$, the energy transfer through spatial turbulent transport increases and the spectral peak as seen in figure 12(*f*) changes to the dominant wavelength. For the case of $c_p/u_* = 25$, due to the fact that the surface waves provide additional energy generation from the mean shear, there is another negative area in the very-near-surface region at the

https://doi.org/10.1017/jfm.2020.246 Published online by Cambridge University Press

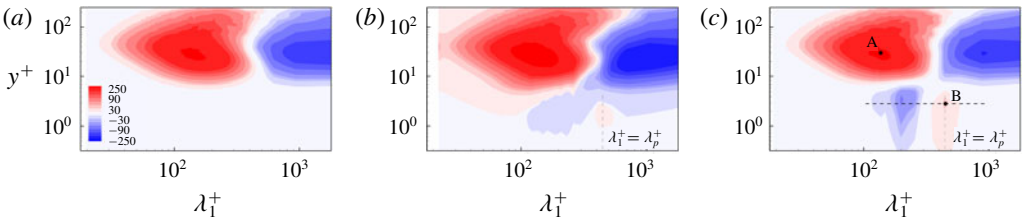


FIGURE 13. The y- and k-premultiplied one-dimensional streamwise spectra of the inter-scale energy transport term, $E_{T_t^\beta,11}$: (*a*) the flat-wall case; (*b*) $c_p/u_* = 2$; (*c*) $c_p/u_* = 25$.

dominant wavelength scale, where the energy is transported outwards via $T_{t,ij}^\alpha$ as seen in figure 12(*i*).

In summary, among the three types of spatial energy transport mechanisms, turbulent energy is transported to the near-surface region by viscous and turbulent transport terms at the dominant wavelength scale for both the slow- and fast-wave cases. Interestingly, the pressure transport direction at the dominant wavelength scale is reversed as the wave age increases, consistent with the opposite near-surface pressure distributions between figures 10(*a*) and 10(*c*).

3.6. *Inter-scale energy transfer*

In addition to the energy transport in the physical space discussed in § 3.5, the energy transfer in the spectral space is also of great importance due to its relation to the energy cascade process, and is discussed in this subsection. Figure 13 shows the premultiplied one-dimensional streamwise spectra of the inter-scale energy transport term in (2.32), $E_{T_t^\beta,11}$. For the flat-wall case, $E_{T_t^\beta,11}$ in figure 13(*a*) shows that the energy-containing large-scale streamwise motion transfers energy to the small-scale motion at $y^+ > 10$, corresponding to the well-known energy cascade process. In the presence of surface waves, it is interesting that the energy of the small-scale streamwise motions is transferred backward to the dominant wavelength scale at $y^+ < 5$ as seen in figure 13(*b*). As the wave age increases to $c_p/u_* = 25$, the inverse cascade in the near-surface region becomes more obvious (figure 13*c*). Because the direction of the inter-scale energy transfer does not change with the wave age, the case of $c_p/u_* = 25$ and the flat-wall case are chosen to illustrate the surface wave effect further.

Considering that the inter-scale energy transport process is complex and features nonlinearity, we resort to triadic interactions at a given wavenumber k_0 to investigate the underlying mechanism. The wavenumbers k_l and k_m satisfying the triadic relationships $k_l + k_m = k_0$ lead to excitation at k_0. The one-dimensional spectrum of the turbulent transport term is rewritten as discretized convolution (Cho *et al.* 2018):

$$E_{T_t,ij}(k_0, y) = \left\langle Re\left\{ \overline{-\hat{u}_i'^*(k_0, y)\frac{\partial}{\partial x_j}\sum_{k_l+k_m=k_0}\hat{u}_i'(k_l, y)\hat{u}_j'(k_m, y)} \right\} \right\rangle_z, \tag{3.2}$$

where k_l and k_m are the streamwise wavenumbers. In the analysis of Cho *et al.* (2018), they focused on the triadic interactions in the spanwise direction. Because in the present problem there exists a characteristic length scale in the streamwise direction associated with the dominant wave and thus a peak in the streamwise

https://doi.org/10.1017/jfm.2020.246 Published online by Cambridge University Press

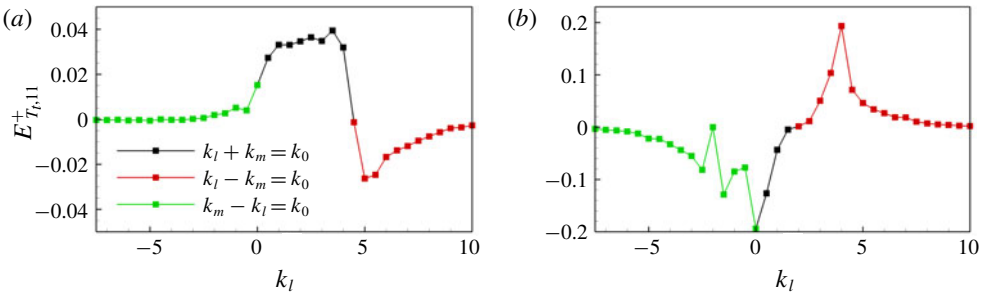


FIGURE 14. Inter-scale turbulent energy transport via triadic interactions at points A (*a*) and B (*b*) marked in figure 13(*c*) for the case of $c_p/u_* = 25$.

spectrum in the near-surface region as shown in figures 13(*b*) and 13(*c*), we choose the streamwise triadic interactions to explore the inter-scale energy transfer. For a positive k_0, the convolution in (3.2) can be written as

$$\sum_{k_l+k_m=k_0} \hat{u}_i'(k_l)\hat{u}_j'(k_m) = \sum_{\substack{k_l+k_m=k_0 \\ k_l,k_m\geqslant 0}} \hat{u}_i'(k_l)\hat{u}_j'(k_m) + \sum_{\substack{k_m-k_l=k_0 \\ k_l,k_m\geqslant 0}} \hat{u}_i'(-k_l)\hat{u}_j'(k_m) + \sum_{\substack{k_l-k_m=k_0 \\ k_l,k_m\geqslant 0}} \hat{u}_i'(k_l)\hat{u}_j'(-k_m). \tag{3.3}$$

Two distinct positive spectral peaks in figure 13(*c*) (marked as points A and B) are chosen as the given streamwise wavenumbers and vertical locations. Figure 14 shows the inter-scale energy transported to the wavenumber k_0 via triadic interactions at the corresponding points A and B. For point A, where the corresponding streamwise wavenumber is $k_0 = 4.5$, the positive turbulent energy transport is dominated by the interactions in the region of $k_l + k_m = k_0$ as shown in figure 14(*a*). This indicates that the energy influx to the motion at the given wavenumber k_0 is mainly from the eddies with larger streamwise sizes, in accordance with the streamwise spectrum of $E_{T_l^\beta,11}$ as shown in figure 13(*c*). The related energy cascade is consistent with the result of Cho *et al.* (2018). For point B in the near-surface region, the energy peak corresponds to the dominant surface wave $k_0 = k_p = 2$. Although point B has the maximum turbulent energy influx in the near-surface region, the corresponding triadic interactions as plotted in figure 14(*b*) are quite different from those of point A. In the vicinity of the surface, the triadic interactions leading to the positive turbulent transport mainly occur in the region of $k_l - k_m > k_0$, indicating that the energy influx at the dominant wavenumber is mediated by the triadic interactions between the turbulent motions that have smaller streamwise sizes than the given one. In addition, the positive peak in figure 14(*b*) corresponds to the second harmonic wavenumber $k_l = 2k_p = 4$. This peak is in accordance with the negative peak in the near-surface region (see figure 13*c*), indicating the second harmonic wave contributes most to the energy influx at k_p.

Next, we take a closer look at the horizontal dashed line in figure 13(*c*), which is at the vertical location of point B. The triadic interactions along this line are expected to explain the inverse energy cascade in the near-surface region discussed above. Figure 15 shows the triadic interactions for different values of k_0 along the dashed line in figure 13(*c*). The value of k_0 ranges from 0.5 to 4.0, with an interval

https://doi.org/10.1017/jfm.2020.246 Published online by Cambridge University Press

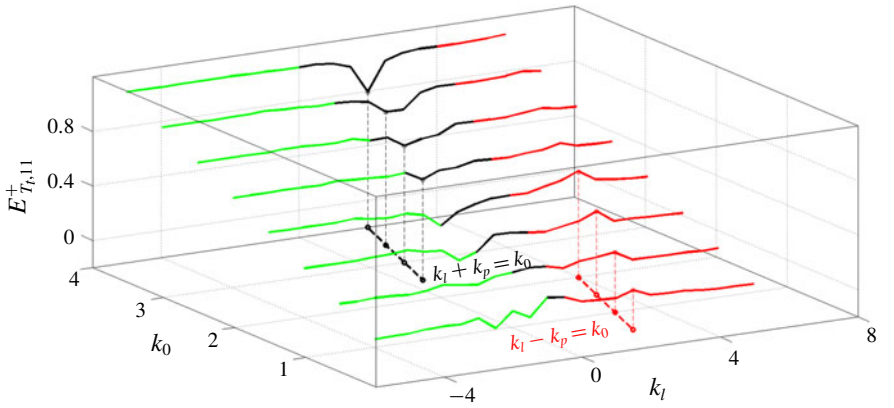


FIGURE 15. Inter-scale turbulent energy transport via triadic interactions along the dashed line marked in figure 13(*c*). The green, black and red lines denote the triadic relationships $-k_l + k_m = k_0$, $k_l + k_m = k_0$ and $k_l - k_m = k_0$, respectively. Note that $k_m = k_p$ on the black and red dashed lines. The value of k_0 ranges from 0.5 to 4.0 with an interval of 0.5. For clarity, each successive interaction curve is raised by 0.15 above the preceding curve at a lower k_0.

of 0.5. Given the streamwise wavenumber k_0, the energy transfer only occurs between pairs of wavenumbers that satisfy the triadic interactions in (3.3). A distinct trough and peak can be observed from figure 15. The corresponding wavenumber pairs (k_0, k_l) are indicated by the black dashed line and red dashed line, respectively. At the trough (black dashed line in figure 15), all the wavenumber pairs (k_0, k_l) satisfy the triadic relationship $k_l + k_m = k_0$ ($k_m = k_p$ here), indicating that the motions of higher wavenumbers $k_0 > k_p$ transfer energy to the dominant wavenumber k_p. For a given streamwise wavenumber $k_0 \leqslant k_p = 2$, a positive peak occurs at k_l satisfying the triadic relationship $k_l - k_m = k_0$ ($k_m = k_p$ here), denoted as the red dashed line in figure 15. This suggests that the energy influx to the given streamwise wavenumber k_0 is caused by the scale interactions between the dominant wavenumber k_p and $k_l > k_0$. Note that $E_{T_t^\beta,11}$ in figure 14(*b*) is positive as k_l varies from 2.5 to 4.0, indicating that these small-scale motions at k_l transfer energy to the dominant wavelength k_p, consistent with the trough in figure 15. In addition to the inter-scale energy transfer related to the dominant wavelength scale of broadband waves, it should be mentioned that relatively weak energy transfer among other scales also exists.

As a summary, the energy transport process including the spatial and inter-scale energy transports is sketched in figure 16. In general, energy is transported from the buffer region to the very-near-surface and outer regions. In the average sense, large-scale motions transfer energy to small-scale motions via T_t^β above the buffer region. In the presence of surface waves, energy transport to the near-surface region via spatial viscous and turbulent transport terms occurs at the dominant wavelength scale for both the slow and fast wave fields, while the pressure transport direction at the dominant wavelength scale changes sign for different wave ages. In the slow-wave case, the energy is transported outwards from the region of $y^+ < 5$ (denoted as red solid arrows), and the opposite process occurs in the fast-wave case (denoted as red dashed arrows). Moreover, energy of small-scale motions is transferred to the dominant wavelength scale via inter-scale transport in the vicinity of the surface.

https://doi.org/10.1017/jfm.2020.246 Published online by Cambridge University Press

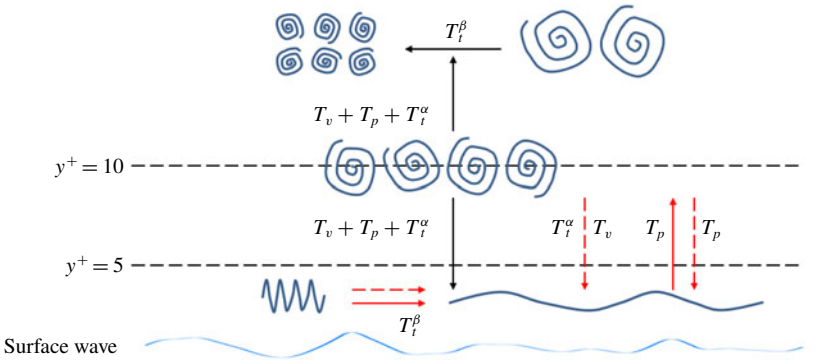


FIGURE 16. Schematic of the spatial and inter-scale energy transfer process in the presence of surface waves. The spiral symbols represent the turbulent motions of different length scales above the buffer region, and the wavy symbols represent the turbulent motions of different length scales in the very vicinity of surface waves. The black solid arrows denote the energy transfer directions in the flat-wall case. The red solid (dashed) arrows denote the directions of the newly emerging energy transfer in the slow (fast) wave field case.

4. Conclusions

In this study, DNS is performed for turbulent flow over surface waves, with the dynamics of the surface waves captured by the HOS method. The initial wave field is given by a broadband wave spectrum, and the effect of the waves on the energy transfer in the overlying turbulent flow is examined. For the slow-wave case of $c_p/u_* = 2$, the dominant wave and its harmonics contribute the most to the energy spectrum in the buffer region, and the original streaky structures are disrupted by the surface waves. In the fast-wave case of $c_p/u_* = 25$, the energy spectrum protrudes from the surface over a wide range of length scales due to the direct contribution of surface waves to the total kinetic energy. As the distance from the wavy surface increases, the wave effect on the energy distribution in the buffer region is greatly attenuated, and the corresponding flow pattern resembles that of flat-wall turbulence.

We have, for the first time, performed a spectral analysis of the two-point correlation transport equation to elucidate the turbulent energy transfer process in the presence of surface waves. Due to the wave motion, the production term has an additional peak in the near-surface region of $y^+ < 20$ as compared with the flat-wall case. Among the transport terms, the effect of viscous transport is confined to the region of $y^+ < 70$, and the process of energy transport from the buffer region to the very-near-surface region at the dominant wavelength scale is enhanced. The turbulent transport contributes the most to the spatial energy transport and affects higher altitudes. Moreover, an additional negative turbulent transport region appears at the dominant wavelength scale in the fast-wave-field case. We have also shown that the pressure-related turbulent energy transfer is dependent on the wave age. For the pressure diffusion term, the energy at the dominant wavelength scale in the region of $y^+ < 10$ is transferred outwards in the slow-wave case of $c_p/u_* = 2$, while the energy in the buffer region is transferred to the near-surface region in the fast-wave case of $c_p/u_* = 25$. For the inter-component energy transfer through the pressure-strain term, the energy is transferred from the streamwise component to the vertical component at the dominant wavelength scale in the region of $y^+ < 10$ in

https://doi.org/10.1017/jfm.2020.246 Published online by Cambridge University Press

the $c_p/u_* = 2$ case, while the energy is transferred from the vertical component to the other two components in the $c_p/u_* = 25$ case. The other part of the nonlinear term, i.e. the inter-scale transport term, transfers energy among different length scales. In general, the large-scale energy-containing motions transfer energy to small-scale motions via the inter-scale transport term, which corresponds to the well-known energy cascade process. Conversely, in the presence of surface waves, energy is transferred from small-scale motions to the turbulent motion at the dominant wavenumber in the very-near-surface region. From the triadic interactions at a given streamwise wavenumber, it is found that the energy influx at the dominant wavelength scale is mainly due to the contribution of the adjacent streamwise wavenumbers, and the turbulent motions at the second harmonic wavenumber contribute the most. In addition to the spectral peak at the dominant wavenumber similar to the monochromatic wave case, the instantaneous field and inter-scale energy transfer also reflect the contributions from the broadband wave components.

The physical picture revealed in this DNS-based, mechanistic study regarding wave effects on the energy transfer process among different length scales in spectral space and different vertical locations in physical space serves as an important first step towards improved modelling for air–sea interactions, e.g. the subgrid-scale modelling of turbulent airflows overlying waves that critically relies on a fundamental understanding of the energy transfer process. Extending the computational framework to more complex cases and developing turbulence models for air–sea interaction applications are beyond the scope of this study, but should be considered in future research.

Acknowledgements

L.-H.W., W.-Y.Z., W.-X.H., C.-X.X. and Z.Z. acknowledge the support of the National Natural Science Foundation of China under grants nos. 11772172, 91752205 and 11490551 and the parallel computing resources provided by Tsinghua National Laboratory for Information Science and Technology. X.H. and L.S. gratefully acknowledge the support of the National Science Foundation and Minnesota Sea Grant. The authors also thank the anonymous reviewers for their valuable comments.

Declaration of interests

The authors report no conflict of interest.

Appendix A. Property of inter-scale turbulent transport

In the spectral analysis of the budget equation (2.17) in wall-bounded turbulent flows, there are multiple ways to decompose the nonlinear turbulent term into spatial and inter-scale parts. In the present study, the decomposition (2.25) is consistent with the definitions used by Mizuno (2016) and Lee & Moser (2019). In curvilinear coordinates, when $r_{\xi_1} = r_{\xi_3} = 0$, the inter-scale turbulent transport term (2.27) satisfies

$$\begin{aligned} T^{\beta}_{t,ij} = & -\overline{u_j'\frac{\partial u_i'u'}{\partial \xi_1}} - \overline{u_i'\frac{\partial u_j u'}{\partial \xi_1}} - \overline{u_j'\frac{\partial u_i'w'}{\partial \xi_3}} - \overline{u_i'\frac{\partial u_j'w'}{\partial \xi_3}} \\ & - \frac{\partial \overline{u_i'u_j'v'}}{\partial \xi_2} + \overline{v'\frac{\partial u_i'u_j'}{\partial \xi_2}} - \overline{\phi_k\frac{\partial u_i'u_j'u_k'}{\partial \xi_2}} + \overline{u_k'\phi_k\frac{\partial u_i'u_j'}{\partial \xi_2}}. \end{aligned} \tag{A 1}$$

https://doi.org/10.1017/jfm.2020.246 Published online by Cambridge University Press

By making use of the chain rule of partial differential (2.6) and the continuity,

$$T^{\beta}_{t,ij} = -\overline{u_i' u_j' \frac{\partial u_k'}{\partial \xi_k}} - \overline{\frac{\partial u' u_i' u_j'}{\partial \xi_1} + \frac{\partial w' u_i' u_j'}{\partial \xi_3}} - \overline{\phi_k u_i' u_j' \frac{\partial u_k'}{\partial \xi_2}} = 0. \tag{A 2}$$

Hence, the two-dimensional spectrum $E_{T_t^{\beta},ij}$, i.e. the Fourier transform of $T^{\beta}_{t,ij}$, inherits the property and satisfies

$$\int\int_0^{\infty} E_{T_t^{\beta},ij}(k_1, \xi_2, k_3)\, \mathrm{d}k_1\, \mathrm{d}k_3 = 0, \quad \forall \xi_2. \tag{A 3}$$

We can therefore interpret $T^{\beta}_{t,ij}$ as the inter-scale energy transfer.

REFERENCES

BELCHER, S. E. & HUNT, J. C. R. 1993 Turbulent shear flow over slowly moving waves. *J. Fluid Mech.* **251**, 109–148.

BLACK, P. G., D'ASARO, E. A., DRENNAN, W. M., FRENCH, J. R., NIILER, P. P., SANFORD, T. B., TERRILL, E. J., WALSH, E. J. & ZHANG, J. A. 2007 Air–sea exchange in hurricanes: synthesis of observations from the coupled boundary layer air–sea transfer experiment. *Bull. Am. Meteorol. Soc.* **88**, 357–374.

BREIVIK, Ø., MOGENSEN, K., BIDLOT, J. R., BALMASEDA, M. A. & JANSSEN, P. A. 2015 Surface wave effects in the NEMO ocean model: forced and coupled experiments. *J. Geophys. Res.* **120**, 2973–2992.

BUCKLEY, M. P. & VERON, F. 2016 Structure of the airflow above surface waves. *J. Phys. Oceanogr.* **46**, 1377–1397.

BUCKLEY, M. P. & VERON, F. 2019 The turbulent airflow over wind generated surface waves. *Eur. J. Mech. (B/Fluids)* **73**, 132–143.

CHEN, S. S., ZHAO, W., DONELAN, M. A. & TOLMAN, H. L. 2013 Directional wind–wave coupling in fully coupled atmosphere–wave–ocean models: results from CBLAST-Hurricane. *J. Atmos. Sci.* **70**, 3198–3215.

CHO, M., HWANG, Y. & CHOI, H. 2018 Scale interactions and spectral energy transfer in turbulent channel flow. *J. Fluid Mech.* **854**, 474–504.

CHOI, H., MOIN, P. & KIM, J. 1993 Direct numerical simulation of turbulent flow over riblets. *J. Fluid Mech.* **255**, 503–539.

CIMARELLI, A., DE ANGELIS, E. & CASCIOLA, C. M. 2013 Paths of energy in turbulent channel flows. *J. Fluid Mech.* **715**, 436–451.

CIMARELLI, A., DE ANGELIS, E., JIMÉNEZ, J. & CASCIOLA, C. M. 2016 Cascades and wall-normal fluxes in turbulent channel flows. *J. Fluid Mech.* **796**, 417–436.

COHEN, J. E. & BELCHER, S. E. 1999 Turbulent shear flow over fast-moving waves. *J. Fluid Mech.* **386**, 345–371.

DOMARADZKI, J. A., LIU, W., HÄRTEL, C. & KLEISER, L. 1994 Energy transfer in numerically simulated wall-bounded turbulent flows. *Phys. Fluids* **6**, 1583–1599.

DOMMERMUTH, D. G. & YUE, D. K. P. 1987 A high-order spectral method for the study of nonlinear gravity waves. *J. Fluid Mech.* **184**, 267–288.

DRUZHININ, O. A., TROITSKAYA, Y. I. & ZILITINKEVICH, S. S. 2012 Direct numerical simulation of a turbulent wind over a wavy water surface. *J. Geophys. Res.* **117**, C00J05.

DUBRULLE, B. 2019 Beyond Kolmogorov cascades. *J. Fluid Mech.* **867**, P1.

EDSON, J., CRAWFORD, T., CRESCENTI, J., FARRAR, T., FREW, N., GERBI, G., HELMIS, C., HRISTOV, T., KHELIF, D., JESSUP, A. *et al.* 2007 The coupled boundary layers and air–sea transfer experiment in low winds. *Bull. Am. Meteorol. Soc.* **88**, 341–356.

GE, M. W., XU, C. X. & CUI, G. X. 2010 Direct numerical simulation of flow in channel with time-dependent wall geometry. *Appl. Math. Mech.* **31**, 97–108.

https://doi.org/10.1017/jfm.2020.246 Published online by Cambridge University Press

GRARE, L., LENAIN, L. & MELVILLE, W. K. 2013 Wave-coherent airflow and critical layers over ocean waves. *J. Phys. Oceanogr.* **43**, 2156–2172.

HAMILTON, J. M., KIM, J. & WALEFFE, F. 1995 Regeneration mechanisms of near-wall turbulence structures. *J. Fluid Mech.* **287**, 317–348.

HAO, X. & SHEN, L. 2019 Wind–wave coupling study using LES of wind and phase-resolved simulation of nonlinear waves. *J. Fluid Mech.* **874**, 391–425.

HARA, T. & SULLIVAN, P. P. 2015 Wave boundary layer turbulence over surface waves in a strongly forced condition. *J. Phys. Oceanogr.* **45**, 868–883.

HASSELMANN, K., BARNETT, T. P., BOUWS, E., CARLSON, H., CARTWRIGHT, D. E., ENKE, K., EWING, J. A., GIENAPP, H., HASSELMANN, D. E., KRUSEMAN, P. *et al.* 1973 Measurements of wind-wave growth and swell decay during the joint north sea wave project (JONSWAP). *Erg. Deutsch. Hydrogr. Z.* **12** (A8), 1–95. Deutches Hydrographisches Institut.

HILL, R. J. 2002 Exact second-order structure-function relationships. *J. Fluid Mech.* **468**, 317–326.

HRISTOV, T. S., MILLER, S. D. & FRIEHE, C. A. 2003 Dynamical coupling of wind and ocean waves through wave-induced air flow. *Nature* **422**, 55–58.

HUSAIN, N. T., HARA, T., BUCKLEY, M. P., YOUSEFI, K., VERON, F. & SULLIVAN, P. P. 2019 Boundary layer turbulence over surface waves in a strongly forced condition: LES and observation. *J. Phys. Oceanogr.* **49**, 1997–2015.

HUSSAIN, A. K. M. F. & REYNOLDS, W. C. 1970 The mechanics of an organized wave in turbulent shear flow. *J. Fluid Mech.* **41**, 241–258.

JIMÉNEZ, J. & PINELLI, A. 1999 The autonomous cycle of near-wall turbulence. *J. Fluid Mech.* **389**, 335–359.

KANG, S. & CHOI, H. 2000 Active wall motions for skin-friction drag reduction. *Phys. Fluids* **12**, 3301.

KIHARA, N., HANAZAKI, H., MIZUYA, T. & UEDA, H. 2007 Relationship between airflow at the critical height and momentum transfer to the traveling waves. *Phys. Fluids* **19**, 015102.

KOLMOGOROV, A. N. 1941*a* The local structure of turbulence in incompressible viscous fluid for very large Reynolds numbers. *Dokl. Akad. Nauk SSSR* **30**, 9–13.

KOLMOGOROV, A. N. 1941*b* Dissipation of energy in the locally isotropic turbulence. *Dokl. Akad. Nauk SSSR* **32**, 16–18.

KRAICHNAN, R. 1971 Inertial-range transfer in two-and three-dimensional turbulence. *J. Fluid Mech.* **47**, 525–535.

KUHN, S., WAGNER, C. & VON ROHR, P. R. 2007 Influence of wavy surfaces on coherent structures in a turbulent flow. *Exp. Fluids* **43**, 251–259.

LEE, M. & MOSER, R. D. 2015 Spectral analysis on Reynolds stress transport equation in high Re wall-bounded turbulence. In *9th International Symposium on Turbulence and Shear Flow Phenomena, Melbourne, Australia, 4A–3*. TSFP9.

LEE, M. & MOSER, R. D. 2019 Spectral analysis of the budget equation in turbulent channel flows at high Reynolds number. *J. Fluid Mech.* **860**, 886–938.

LIU, Y., YANG, D., GUO, X. & SHEN, L. 2010 Numerical study of pressure forcing of wind on dynamically evolving water waves. *Phys. Fluids* **22**, 041704.

LUMLEY, J. L. 1964 Spectral energy budget in wall turbulence. *Phys. Fluids* **7**, 190–196.

MARATI, N., CASCIOLA, C. M. & PIVA, R. 2004 Energy cascade and spatial fluxes in wall turbulence. *J. Fluid Mech.* **521**, 191–215.

MARUSIC, I., MATHIS, R. & HUTCHINS, N. 2010 High Reynolds number effects in wall turbulence. *Intl J. Heat Fluid Flow* **31**, 418–428.

MASTENBROEK, C., MAKIN, V. K., GARAT, M. H. & GIOVANANGELI, J. P. 1996 Experimental evidence of the rapid distortion of turbulence in the air flow over water waves. *J. Fluid Mech.* **318**, 273–302.

MEI, C. C., STIASSNIE, M. & YUE, D. K. P. 2005 *Theory and Applications of Ocean Surface Waves: Nonlinear Aspects*. World Scientific.

MENEVEAU, C. & KATZ, J. 2000 Scale-invariance and turbulence models for large-eddy simulation. *Annu. Rev. Fluid Mech.* **32**, 1–32.

MILES, J. W. 1957 On the generation of surface waves by shear flows. *J. Fluid Mech.* **3**, 185–204.

https://doi.org/10.1017/jfm.2020.246 Published online by Cambridge University Press

MIZUNO, Y. 2016 Spectra of energy transport in turbulent channel flows for moderate Reynolds numbers. *J. Fluid Mech.* **805**, 171–187.

PHILLIPS, O. M. 1957 On the generation of waves by turbulent wind. *J. Fluid Mech.* **2**, 417–445.

PLANT, W. J. 1982 A relationship between wind stress and wave slope. *J. Geophys. Res.* **87**, 1961–1967.

RICHARDSON, L. F. 1922 *Weather Prediction by Numerical Process*. Cambridge University Press.

RUTGERSSON, A. & SULLIVAN, P. P. 2005 The effect of idealized water waves on the turbulence structure and kinetic energy budgets in the overlying airflow. *Dyn. Atmos. Ocean* **38**, 147–171.

SHEN, L., ZHANG, X., YUE, D. K. P. & TRIANTAFYLLOU, M. S. 2003 Turbulent flow over a flexible wall undergoing a streamwise travelling wave motion. *J. Fluid Mech.* **484**, 197–221.

SIDDIQUI, M. K. & LOEWEN, M. R. 2007 Characteristics of the wind drift layer and microscale breaking waves. *J. Fluid Mech.* **573**, 417–456.

SMITS, A. J., MCKEON, B. J. & MARUSIC, I. 2011 High-Reynolds number wall turbulence. *Annu. Rev. Fluid Mech.* **43**, 353–375.

SULLIVAN, P. P. & MCWILLIAMS, J. C. 2010 Dynamics of winds and currents coupled to surface waves. *Annu. Rev. Fluid Mech.* **42**, 19–42.

SULLIVAN, P. P., MCWILLIAMS, J. C. & MOENG, C. H. 2000 Simulation of turbulent flow over idealized water waves. *J. Fluid Mech.* **404**, 47–85.

SULLIVAN, P. P., MCWILLIAMS, J. C. & PATTON, E. G. 2014 Large-eddy simulation of marine atmospheric boundary layers above a spectrum of moving waves. *J. Atmos. Sci.* **71**, 4001–4027.

TANAKA, M. 2001 A method of studying nonlinear random field of surface gravity waves by direct numerical simulation. *Fluid Dyn. Res.* **28**, 41–60.

THAIS, L. & MAGNAUDET, J. 1996 Turbulent structure beneath surface gravity waves sheared by the wind. *J. Fluid Mech.* **328**, 313–344.

VASSILICOS, J. C. 2015 Dissipation in turbulent flows. *Annu. Rev. Fluid Mech.* **47**, 95–114.

XIAO, W., LIU, Y., WU, G. & YUE, D. K. P. 2013 Rogue wave occurrence and dynamics by direct simulations of nonlinear wave-field evolution. *J. Fluid Mech.* **720**, 357–392.

YANG, D., MENEVEAU, C. & SHEN, L. 2013 Dynamic modelling of sea-surface roughness for large-eddy simulation of wind over ocean wavefield. *J. Fluid Mech.* **726**, 62–99.

YANG, D., MENEVEAU, C. & SHEN, L. 2014 Large-eddy simulation of offshore wind farm. *Phys. Fluids* **26**, 025101.

YANG, D. & SHEN, L. 2009 Characteristics of coherent vortical structures in turbulent flows over progressive surface waves. *Phys. Fluids* **21**, 125106.

YANG, D. & SHEN, L. 2010 Direct-simulation-based study of turbulent flow over various waving boundaries. *J. Fluid Mech.* **650**, 131–180.

YANG, D. & SHEN, L. 2011 Simulation of viscous flows with undulatory boundaries: Part II. Coupling with other solvers for two-fluid computations. *J. Comput. Phys.* **230**, 5510–5531.

YANG, D. & SHEN, L. 2017 Direct numerical simulation of scalar transport in turbulent flows over progressive surface waves. *J. Fluid Mech.* **819**, 58–103.

ZHANG, W. Y., HUANG, W. X. & XU, C. X. 2019 Very large-scale motions in turbulent flows over streamwise traveling wavy boundaries. *Phys. Rev. Fluids* **4**, 054601.

ZHOU, J., ADRIAN, R. J., BALACHANDAR, S. & KENDALL, T. M. 1999 Mechanisms for generating coherent packets of hairpin vortices in channel flow. *J. Fluid Mech.* **387**, 353–396.

https://doi.org/10.1017/jfm.2020.246 Published online by Cambridge University Press